Context-Dependent Reconfiguration And Spatial Reorganisation Of The Mir-199A-5P/Xiap Axis In High-Grade Serous Ovarian Cancer

Teresa Muñoz-Galdeano[1],†,; Davis Reigada[1]; Manuel Nieto-Díaz[1]; Magda Palka Kotlowska[1]; Lorena González Gea[2]; María García Peña[2]; Belén Santacruz[2]; Guillermo Iglesias[3]; Rodrigo M. Maza[1],†,

[1] Molecular Neuroprotection Group, Research Unit, National Hospital for Paraplegics (SESCAM), Toledo, Spain
[2] Department of Obstetrics and Gynecology, Hospital Universitario de Torrejón, Madrid, Spain
[3] Department of Information Systems, Universidad Politécnica de Madrid, Madrid, Spain

† These authors contributed equally to this work.

Corresponding authors.

Correspondence:
Teresa Muñoz-Galdeano (tmunozd@sescam.jccm.es; ORCID: 0000-0003-3526-819X
Rodrigo M. Maza (rodrigom@sescam.jccm.es; ORCID: 0000-0002-7249-9205

ABSTRACT

Background
High-grade serous ovarian cancer (HGSOC) remains a leading cause of gynaecological cancer mortality, largely owing to late diagnosis and the emergence of platinum resistance. A defining feature of resistant disease is impaired apoptotic execution despite persistent survival signalling. XIAP is a key inhibitor of caspase activity, and microRNAs are important modulators of stress-response pathways; however, the functional relationship between individual miRNAs and their targets may vary across cellular states.

Methods
We investigated the miR-199a-5p/XIAP axis by integrating (i) cross-species structural and CLIP-informed support for miR-199a-5p binding to the XIAP 3'UTR, (ii) functional perturbation in paired cisplatin-sensitive (A2780) and cisplatin-resistant (A2780cis) ovarian cancer cell models, and (iii) spatial characterisation in human ovarian tissue using multiplex fluorescence in situ hybridisation and immunofluorescence. Quantitative image analysis was used to assess signal distribution and co-localisation at single-cell resolution.

Results
miR-199a-5p did not show a uniform repressive relationship with XIAP across cellular contexts. In cisplatin-sensitive cells, miR-199a-5p was consistent with basal XIAP repression and was associated with enhanced apoptotic responses following cisplatin exposure. In resistant cells, this relationship was attenuated, and cisplatin treatment was accompanied by divergence between XIAP levels and apoptotic readouts. Spatial analysis of human FFPE specimens showed tumour-associated reorganisation of this axis. Non-neoplastic ovary displayed compartmental segregation, with XIAP enriched in epithelial

structures and miR-199a-5p relatively restricted to stromal regions. In HGSOC, this organisation was altered, with broader miR-199a-5p distribution, greater spatial overlap with XIAP, and a distinct perinuclear, occasionally nuclear-associated, miR-199a-5p pattern not observed in control tissue.

Conclusions
These findings indicate that the functional relationship between miR-199a-5p and XIAP is context-dependent and altered in cisplatin-resistant states. The identification of a tumour-associated spatial phenotype in human HGSOC underscores the value of spatially resolved approaches for understanding regulatory heterogeneity and supports their potential utility in biomarker development and in the identification of therapeutic vulnerabilities linked to platinum-resistant disease.

Clinical Trial Registration
Not applicable.

BACKGROUND

Ovarian cancer mortality is determined less by lack of initial chemosensitivity than by the high rate of relapse and the clinical challenge of platinum resistance, for which reliable predictive and early-stage biomarkers remain limited. Recent clinical studies indicate that platinum resistance is not driven by a single mechanism, but represents a multifactorial and context-dependent phenotype, with particularly poor outcomes in primary platinum-resistant disease [1]. At the same time, biomarker development remains limited by the difficulty of identifying biologically relevant changes early enough to inform clinical decision-making [2].

One important factor underlying this limitation is the spatial organisation of the tumour. High-grade serous ovarian cancer shows marked intratumoral heterogeneity, with spatially distinct subclones and microenvironmental niches that influence drug response and tumour evolution [3]. In keeping with this, recent spatial profiling studies have shown that clinically relevant response regions may differ transcriptionally despite similar histological appearance, highlighting the value of spatially resolved molecular analysis in HGSOC [4].

Within this setting, apoptotic competence is an important determinant of treatment response. Multiple models of resistance point to impaired apoptosis as a central mechanism of platinum failure, and inhibitor-of-apoptosis proteins (IAPs) are key regulators of this process because they directly suppress caspase activation and integrate survival signalling pathways [5,6]. In ovarian cancer, XIAP has been specifically linked to platinum-resistant phenotypes, supporting the need to examine its regulation rather than abundance alone [5,7].

MicroRNAs may represent an additional regulatory layer in this context, but their functional interpretation is often limited by reliance on bulk measurements. Although miRNA dysregulation is widely recognised as part of resistance-associated circuitry, bulk

profiling cannot determine whether miRNA–target relationships are preserved, spatially redistributed or reorganised at subcellular level [8]. This limitation is particularly relevant because mature miRNAs may localise outside the cytoplasm, including within nuclear compartments, where they can participate in gene regulatory processes [9,10].

Among these, miR-199a-5p has been associated with tumour-suppressive functions in ovarian cancer and linked to recurrence- and chemoresistance-related settings, including recent evidence that restoration of miRNA regulatory networks can modify resistant phenotypes [11]. Additional studies support a role for miR-199a-5p in ovarian cancer biology across different microenvironmental contexts [12]. Our laboratory previously identified XIAP as a direct target of miR-199a-5p in a mammalian experimental system [13], providing a mechanistic basis for examining how this interaction behaves in a clinically relevant setting and supporting the broader biological relevance of this regulatory axis.

In the present study, we examined whether the miR-199a-5p/XIAP axis contributes to cisplatin response and whether this relationship is altered in resistant states. To address this, we combined CLIP-informed in silico prediction, functional analysis in paired cisplatin-sensitive and cisplatin-resistant ovarian cancer cell models, and spatially resolved miRNA–protein mapping in human FFPE tissue using multiplex miRNA FISH and XIAP immunofluorescence. By integrating mechanistic analysis with tissue-level spatial information, this study evaluates the miR-199a-5p/XIAP relationship as a context-dependent regulatory interaction whose spatial organisation may be relevant to platinum resistance in HGSOC.

MATERIALS AND METHODS

In silico miRNA–mRNA interaction analysis

The accessibility of the miR-199a-5p binding site within the human XIAP 3′ untranslated region (3′UTR) was evaluated using the STarMir prediction platform [14], which implements logistic regression models trained on high-throughput crosslinking immunoprecipitation (CLIP) datasets. Analyses were performed using the STarMir web server (Wadsworth Center, New York, NY, USA; https://sfold.wadsworth.org/cgi-bin/starmirtest2.pl; accessed 5 November 2023). The mature hsa-miR-199a-5p sequence was used as query, and the human XIAP 3′UTR sequence was entered manually. Predictions were generated using the human V-CLIP-based model, with species set to Homo sapiens and the target region restricted to the 3′UTR. Output parameters included hybridisation energy (ΔG_hybrid), seed-pairing configuration, site accessibility scores and the composite LogitProb value, which estimates the probability of functional miRNA–mRNA interaction.

Local RNA secondary structure surrounding the predicted binding site was modelled using RNAfold from the ViennaRNA Package (Institute for Theoretical Chemistry, University of Vienna, Vienna, Austria). Human and murine XIAP 3′UTR sequences were

analysed under identical conditions to assess conservation of structural features. Minimum free-energy (MFE) and centroid structures were examined to evaluate accessibility of the predicted binding region.

Patient samples, FFPE processing and cell culture

Formalin-fixed paraffin-embedded (FFPE) ovarian tissue samples were obtained from the Department of Obstetrics and Gynecology, Hospital Universitario de Torrejón (Madrid, Spain). The cohort included ten high-grade serous ovarian carcinoma (HGSOC) specimens and ten non-neoplastic control tissues derived from oophorectomy or hysterectomy performed for benign gynaecological conditions. Representative haematoxylin and eosin (H&E)-stained sections were reviewed by a certified pathologist to confirm histopathological diagnosis. For each FFPE block, a 3 mm punch biopsy was taken from the selected region of interest. All samples were anonymised, numerically coded and analysed in a blinded manner.

Human ovarian carcinoma cell lines A2780 (ECACC 93112519; RRID:CVCL_0134) and its cisplatin-resistant derivative A2780cis (ECACC 93112517; RRID:CVCL_0135) were obtained from the Cell Bank of the Centro de Instrumentación Científica (CIC), University of Granada (Granada, Spain). Cell lines were authenticated by short tandem repeat (STR) profiling and confirmed to be free of bacterial, fungal and mycoplasma contamination. Cells were maintained under biosafety level 2 conditions.

A2780 cells were cultured in RPMI-1640 medium (Gibco, Thermo Fisher Scientific, Waltham, MA, USA) supplemented with 2 mM L-glutamine and 10% fetal bovine serum (FBS; Gibco, Thermo Fisher Scientific). A2780cis cells were maintained in the same medium supplemented with 1 μM cisplatin to preserve the resistant phenotype. Cells were incubated at 37 °C in a humidified atmosphere containing 5% CO_2. For passaging, cells at 70–80% confluence were detached using 0.25% trypsin–EDTA (Gibco, Thermo Fisher Scientific) and reseeded at ratios of 1:3–1:6 for A2780 and 1:5–1:20 for A2780cis. After thawing, A2780cis cells were maintained in cisplatin-free medium for 24–48 h prior to re-exposure to cisplatin.

Transfection and drug treatment

Transient transfections were performed using DharmaFECT-4 reagent (Dharmacon, Horizon Discovery, Waterbeach, UK) according to the manufacturer's instructions. Cells were transfected at approximately 75–80% confluence for 24 h with 50 nM miRIDIAN hsa-miR-199a-5p mimic (miRBase accession: MIMAT0000231; Dharmacon, cat. no. C-300533-03-0002; sequence: 5′-CCCAGUGUUCAGACUCCUGUUC-3′) or a non-targeting negative control mimic (cel-miR-67-3p; miRBase accession: MIMAT0000039; Dharmacon, cat. no. CN-001000-01-05; sequence: 5′-UCACAACCUCCUAGAAAGAGUAGA-3′). Following transfection, cells were treated with 12.5 μM cisplatin (cis-diamminedichloroplatinum II; Sigma-Aldrich, St. Louis, MO, USA; cat. no. P4394) for 24 h under standard culture conditions. Control cells were processed in parallel and maintained in cisplatin-free medium.

RNA extraction and quantitative PCR (RT–qPCR)

Basal expression levels of XIAP mRNA and miR-199a-5p were assessed in untreated A2780 and A2780cis cells. Total RNA was extracted from confluent cultures using QIAzol Lysis Reagent (Qiagen, Hilden, Germany; cat. no. 79306), followed by purification with the miRNeasy Mini Kit (Qiagen; cat. no. 217004), according to the manufacturer's instructions. RNA concentration and purity were determined using a NanoDrop ND-1000 spectrophotometer (Thermo Fisher Scientific, Waltham, MA, USA).

For miR-199a-5p quantification, 10 ng of total RNA were reverse-transcribed and amplified using a TaqMan MicroRNA assay (Applied Biosystems, Thermo Fisher Scientific, Foster City, CA, USA; assay ID 000498). U6 small nuclear RNA (assay ID 001973) was used as endogenous control. For XIAP mRNA analysis, 1 µg of total RNA was treated with DNase I (Roche, Basel, Switzerland; cat. no. 10104159001) and reverse-transcribed using Moloney murine leukaemia virus reverse transcriptase (M-MLV; Invitrogen, Thermo Fisher Scientific; cat. no. 28025013) and random primers (Roche; cat. no. 48190011). Quantitative PCR was performed using TaqMan Universal PCR Master Mix (Applied Biosystems; cat. no. 4324020) with gene-specific probes for XIAP (Hs00180269_m1) and miR-199a-5p (000498). 18S rRNA (Hs99999901_s1) and U6 RNA (001973) were used as endogenous controls for mRNA and miRNA normalisation, respectively. Amplification was carried out on a TaqMan 7900HT Fast Real-Time PCR System (Applied Biosystems) under standard cycling conditions (10 min at 95 °C, followed by 40 cycles of 15 s at 95 °C and 1 min at 60 °C).

All experiments were performed with three independent biological replicates and three technical replicates per condition. Relative expression levels were calculated using the $2^{-\Delta\Delta Ct}$ method as described by Livak and Schmittgen [15], with error propagation performed according to Headrick [16]. Results were expressed as fold change in A2780cis relative to A2780, including 95% confidence intervals.

Protein extraction and immunoblotting

For protein expression analyses, A2780 and A2780cis cells were seeded in 6-well plates (2.5×10^5 cells per well) and cultured to approximately 80% confluence. Depending on the experimental condition, cells were either left untreated or transfected with miR-199a-5p or negative control mimics for 24 h, followed, where indicated, by treatment with 12.5 µM cisplatin for an additional 24 h.

Cells were harvested by mechanical detachment and lysed in RIPA buffer (Thermo Fisher Scientific, Waltham, MA, USA; cat. no. 89900) supplemented with cOmplete™ EDTA-free protease inhibitor cocktail (Merck, Darmstadt, Germany; cat. no. 11873580001). Lysates were incubated for 30 min at 4 °C and clarified by centrifugation at 12,000 × g for 10 min at 4 °C. Protein concentration was determined using the Pierce™ BCA Protein Assay Kit (Thermo Fisher Scientific; cat. no. 23225). Equal amounts of total protein (50 µg per lane) were mixed with Laemmli sample buffer (Bio-Rad, Hercules, CA, USA; cat. no. 1610747) containing β-mercaptoethanol (Sigma-Aldrich, St. Louis, MO, USA; cat. no. M6250) and boiled for 5 min at 100 °C. Proteins were resolved by SDS–PAGE and transferred onto PVDF membranes (Immobilon-P, 0.2 µm; Merck Millipore; cat. no. IPVH00005). Membranes were blocked for 1 h at room temperature in 5% non-fat dry milk diluted in TBS-T and incubated overnight at 4 °C with primary antibodies diluted in blocking

solution. After washing, membranes were incubated for 90 min at room temperature with HRP-conjugated secondary antibodies (see Table 1 for antibody details). Signals were detected using SuperSignal™ West Pico PLUS substrate (Thermo Fisher Scientific; cat. no. 34580) and visualised with an ImageScanner III system (GE Healthcare). Image acquisition was performed under non-saturating conditions using instrument settings selected to prevent signal saturation. Band intensities were quantified using ImageJ v1.54p (NIH, Bethesda, MD, USA). Antibodies detected bands at the expected molecular weights without evidence of relevant non-specific signal. The number of independent biological replicates for each experiment is indicated in the corresponding figure legends.

Table 1. Primary and secondary antibodies used in this study

Antibody	Reference
Primary antibodies for Immunoblot	
anti-XIAP	BD Biosciences (Franklin Lakes, NJ, USA) Cat# 610716, RRID:AB_398039)
anti-β-Actin	BD Biosciences (Franklin Lakes, NJ, USA); Cat# 612656, RRID:AB_2289199
Primary antibodies for Immunofluorescence	
anti-XIAP	(Abcam Cat# ab21278, RRID:AB_446157)
anti-Caspase 3 fragment	(Cell Signaling Technology Cat# 94530, RRID:AB_3076239)
Primary antibody for FISH	
Alkaline phosphatase–conjugated sheep anti-digoxigenin	Sigma-Aldrich Cat# 11093274910, RRID:AB_2734716
Secondary antibodies for Immunoblot	
HRP-conjugated goat anti-rabbit	Cell Signaling Technology (Danvers, MA, USA); Cat# 7074, RRID:AB_2099233
HRP-conjugated goat anti-mouse	Cell Signaling Technology; Cat# 7076, RRID:AB_330924
Secondary antibodies for Immunofluorescence	
Alexa Fluor 488 goat anti-mouse, highly cross-adsorbed	Molecular Probes (Eugene, OR, USA); Cat# A11029, RRID:AB_138404

Fluorescence in situ hybridisation (FISH) in human ovarian tissue

Detection of miR-199a-5p in FFPE human ovarian tissue sections was performed using an adaptation of the protocol described by Søe et al. [17]. All solutions were prepared using DEPC-treated water (1:1000; Merck KGaA, Darmstadt, Germany). Slides were incubated at 65 °C for 2 h, deparaffinised in xylene (15 min ×2) and rehydrated through graded ethanol (100% ×2, 80% and 70%) before immersion in distilled water. Antigen retrieval was performed in 250 mM EDTA at 97 °C for 20 min using a PT Link system (Agilent Technologies, Santa Clara, CA, USA). Tissue digestion was then carried out with pepsin solution (ZytoVision, Bremerhaven, Germany) for 30 min at 37 °C. DIG-labelled LNA probes specific for miR-199a-5p or the negative control cel-miR-67 (Eurogentec, Seraing, Belgium) were applied to each section. Probes were denatured at 85 °C for 15 min and hybridised overnight at 37 °C. After hybridisation, slides were washed in 0.4× SSC containing 0.3% NP-40 at 75 °C for 2 min, followed by 0.2× SSC containing 0.1% NP-40 for 1 min at room temperature. Sections were blocked for 15 min at 37 °C in 5% horse serum and 1% BSA in PBS-T-DEPC, and then incubated with alkaline phosphatase-conjugated anti-digoxigenin antibody (Table 1) for 20 min at 37 °C. Signal detection was performed using the Vector Blue Alkaline Phosphatase Substrate Kit (Vector Laboratories, Newark, CA, USA), according to the manufacturer's instructions. Images were acquired using a fully motorised Olympus IX83 microscope (Olympus, Tokyo, Japan) equipped with CellSens Dimensions software v4.1.1 (Olympus).

Fluorescence in situ hybridisation (FISH) in cultured ovarian cancer cells

FISH analysis of miR-199a-5p was performed in A2780 and A2780cis ovarian carcinoma cells grown on sterile glass coverslips, following an adapted protocol optimised for DIG-labelled LNA probes (Eurogentec, Seraing, Belgium) under RNase-free conditions. All solutions were prepared using DEPC-treated water (1:1000; Merck KGaA, Darmstadt, Germany). Cells were washed twice with PBS-DEPC and permeabilised with PBS containing 0.1% Tween-20 for 15 min at room temperature. Acetylation was performed using freshly prepared buffer containing triethanolamine (1.3%), HCl (0.06%) and acetic anhydride (0.25%, added immediately before use) in DEPC-treated water, followed by washing in PBS-DEPC. For hybridisation, cells were preincubated for 30 min at 65 °C in a 1:1 mixture of miRCURY LNA hybridisation buffer (Qiagen) and DEPC-treated water, and subsequently incubated for 1 h at 65 °C with DIG-labelled LNA probes specific for miR-199a-5p or the negative control cel-miR-67 (dilution 1:100; ~200 nM). Probes were denatured at 80 °C for 5 min immediately prior to use. Post-hybridisation washes were performed sequentially in 5×, 1× and 0.1× SSC at 65 °C, followed by a final wash in 0.1× SSC at room temperature. Samples were then blocked for 15 min at 37 °C in 2% horse serum and 1% BSA in PBS-T. Detection was carried out using an alkaline phosphatase-conjugated anti-digoxigenin antibody, followed by chromogenic development with the Vector Blue Alkaline Phosphatase Substrate Kit (Vector Laboratories, Newark, CA, USA) according to the manufacturer's instructions. Images were acquired using an epifluorescence microscope (DM5000B, Leica Microsystems GmbH, Wetzlar, Germany) with a 20× objective, capturing five fields per sample. No signal was detected in negative control conditions.

Table 2. DIG-labelled probe sequences used for miR-199a-5p FISH analysis.
Sequences for the miR-199a-5p and negative control cel-miR-67 probes are shown. Probes were designed according to Søe et al.15 and contain 2′-O-methyl RNA nucleotides ([]) and locked nucleic acid (LNA) nucleotides ({}).

Probe	Sequence
Negative Control	5′-DIG-{G}[T]{GU}[A]{AC}[A]{CG}[T]{CU}[A]{UA}[C]{GC}[C]{CA}-3′
miR-199a-5p	5′-DIG-{G}[AA]{C}[AG]{G}[UA]{G}[UC]{T}[GA]{A}[CA]{C}[UG]{GG}-3′

CELL DEATH ASSAYS

MTT cell viability assay

Cell viability was assessed using the 3-(4,5-dimethylthiazol-2-yl)-2,5-diphenyltetrazolium bromide (MTT) assay as a measure of mitochondrial metabolic activity. A2780 and A2780cis cells were seeded in clear 96-well plates at a density of 2×10^4 cells per well and allowed to adhere overnight. Transfection and treatment were performed as described above, using miR-199a-5p or negative control mimics, followed by exposure to 12.5 μM cisplatin or vehicle for 24 h.
MTT reagent (Merck KGaA, Darmstadt, Germany; cat. no. M5655) was added directly to the culture medium at a final concentration of 0.5 mg/mL, and cells were incubated for 3 h at 37 °C protected from light. Formazan crystals were solubilised with 100 μL HCl:isopropanol solution (1:500; Merck KGaA). Absorbance was measured at 570 nm with background correction at 660 nm using an Infinite M200 Pro microplate reader (Tecan Group Ltd., Männedorf, Switzerland). Cell viability was expressed as normalised absorbance relative to the untreated negative control condition.

Propidium iodide (PI) staining assay

Late cell death was assessed by propidium iodide (PI) staining as a measure of plasma membrane integrity. Following transfection and treatment, A2780 and A2780cis cells grown on sterile glass coverslips were incubated for 30 min at 37 °C in warm phosphate-buffered saline (PBS) containing 0.4 μg/mL propidium iodide (Sigma-Aldrich, St. Louis, MO, USA; cat. no. P4170), protected from light.
Cells were then washed twice with PBS and mounted using DAKO Fluorescence Mounting Medium (Agilent Technologies, Santa Clara, CA, USA; cat. no. S3023). Fluorescence images were acquired using an epifluorescence microscope (DM5000B, Leica Microsystems GmbH, Wetzlar, Germany) equipped with a 20× objective and a Leica DFC 3000 G digital camera. The percentage of PI-positive cells relative to the total number of nuclei was used as an index of late, irreversible cell death.

Caspase-3/7 activity assay

Effector caspase activity was assessed at single-cell level using the CellEvent™ Caspase-3/7 Green Detection Reagent (Thermo Fisher Scientific, Waltham, MA, USA; cat. no. C10423). Following transfection and treatment, A2780 and A2780cis cells grown on sterile glass coverslips were incubated for 30 min at 37 °C in warm phosphate-buffered saline (PBS) containing 2.5 μM CellEvent™ reagent and 10% fetal bovine serum, protected from light. After incubation, the reagent was removed and cells were fixed with 4% paraformaldehyde for 15 min at room temperature. Cells were then washed three times in PBS, with DAPI (Thermo Fisher Scientific; cat. no. D1306) added during the first wash for nuclear counterstaining. Samples were mounted using DAKO Fluorescence Mounting Medium (Agilent Technologies, Santa Clara, CA, USA; cat. no. S3023). Fluorescence images were acquired using an epifluorescence microscope (DM5000B, Leica Microsystems GmbH, Wetzlar, Germany) equipped with a 20× objective and a Leica DFC 3000 G digital camera. The proportion of caspase-3/7-positive cells relative to the total number of nuclei was used as an index of effector caspase activation.

IMAGE ANALYSIS

In vitro experiments

Quantitative image analysis of propidium iodide staining, caspase-3/7 activity, and basal XIAP and miR-199a-5p fluorescence was performed using QuPath v0.4.3. Nuclei were detected based on DAPI fluorescence using the Cell detection algorithm with the following parameters: detection channel 3 (DAPI), background radius 15 px, median filter radius 2 px, sigma 8 px, minimum area 10 px^2, maximum area 5000 px^2, threshold 1000, and cell expansion 5 μm to generate a cytoplasmic measurement area while retaining the nucleus within the detected object. The Make measurements option was enabled. XIAP immunofluorescence and caspase-3/7 activity were quantified in the FITC/Alexa 488 channel, whereas PI staining was analysed in the red channel. A total of 556 A2780 cells and 564 A2780cis cells were analysed for basal fluorescence measurements (n = 3 independent experiments). For PI and caspase-3/7 assays, approximately 1,500 cells per condition were analysed across five non-overlapping fields per replicate (n = 4 independent experiments). Mean fluorescence intensity values were exported for downstream statistical analysis.

Human tissue FISH/IF analysis

FISH/IF images were acquired using a fully motorised Olympus IX83 microscope (Olympus, Tokyo, Japan) with CellSens Dimensions software v4.1.1. Image analysis was performed in QuPath v0.4.3 using a custom macro. Ten regions of interest (ROIs; 750 × 750 μm) were defined per sample to ensure representative tissue coverage. Nuclei were automatically detected based on DAPI staining, and fluorescence intensities were quantified per detected object in the FITC (XIAP) and Cy5 (miR-199a-5p) channels. ROI-level CSV files were exported for downstream analysis.

Colocalisation analysis

Colocalisation metrics were computed in a blinded manner using R (≥4.2) within the tidyverse framework. Channel-specific thresholds were defined using the 25th percentile of per-cell intensity distributions. For each ROI, Pearson correlation coefficients and Manders' overlap coefficients (M1 and M2) were calculated from per-cell mean intensities. In addition, cross-correlation descriptors exported from QuPath (CCF_MAX, CCF_MIN, K1, K2 and FWHM) were incorporated. ROI-level data were aggregated to generate a single mean value per image by averaging across the ten ROIs. Both ROI-level and image-level datasets were exported for statistical analysis, with group labels masked during processing to preserve blinding.

Statistical analysis

Statistical analyses were performed using GraphPad Prism and R software (≥4.2), and were selected according to the experimental design and data structure. Linear mixed-effects models (LMMs) were used as the primary analytical framework for functional assays, including cell viability (MTT), membrane integrity (propidium iodide, PI), caspase-3/7 activation, and XIAP protein levels under treatment. In these models, transfection status (miR-199a-5p) and cisplatin treatment, as well as their interaction, were included as fixed effects, while experimental day was incorporated as a random intercept to account for inter-experimental variability. Fixed effects were evaluated using Satterthwaite's approximation for degrees of freedom, as implemented in the lmerTest package. Where appropriate, post hoc pairwise comparisons were adjusted using Tukey's method to control for multiple testing.

For two-group comparisons under basal conditions, parametric Student's t-tests were applied to RT–qPCR measurements, whereas basal FISH/IF fluorescence intensities were analysed using Mann–Whitney U tests. A paired one-tailed t-test was used for densitometric analysis of basal XIAP immunoblots following miR-199a-5p transfection in matched experiments, based on a pre-specified a priori directional hypothesis of XIAP reduction. For human tissue analyses and single-cell intensity distributions that did not meet normality and/or homoscedasticity assumptions, non-parametric or variance-robust tests were applied. Specifically, Mann–Whitney U tests were used for M1, K1 and FWHM metrics, whereas Welch's t-tests were used for Pearson correlation, M2, CCF_MAX, CCF_MIN and K2 parameters. Multivariate structure within the colocalisation dataset was further explored by principal component analysis (PCA). In silico prediction of miR-199a-5p binding to XIAP mRNA was performed using STarMir, based on CLIP-informed logistic regression models. Data are presented as mean ± SEM calculated from independent experiments, while statistical significance was assessed using the fitted mixed-effects models unless otherwise specified. For image-based assays, measurements from multiple fields and cells within each experiment were aggregated at the experimental level, and each independent experiment was treated as one biological replicate for statistical inference. All statistical tests were two-sided unless otherwise specified, and statistical significance was defined as $p < 0.05$.

RESULTS

XIAP is a conserved target of miR-199a-5p

In our previous study [13], miR-199a-5p was identified among seven microRNAs predicted to target the 3′UTR of rat XIAP mRNA and was functionally validated as a direct regulator in a mammalian experimental system. To assess whether this interaction was likely to be conserved in the present human ovarian cancer context, we first examined target-site accessibility and duplex stability. PITA-based analysis showed canonical seed pairing and favourable hybridisation energies for miR-199a-5p within the XIAP 3′UTR in both human and mouse (ΔG_hybrid = −15.4 and −15.2 kcal/mol, respectively; Fig. 1A,B). We next applied STarMir, a CLIP-informed prediction framework incorporating features derived from experimentally mapped miRNA–mRNA interactions in human [18] and mouse [19] datasets.. This analysis identified accessible miR-199a-5p binding sites in both species, with LogitProb values above the functional threshold (>0.5) in human (0.543) and mouse (0.594) (Fig. 1C). RNAfold modelling further supported structural accessibility of the predicted binding region (Fig. 1D). Together, these data support a thermodynamically favourable and evolutionarily conserved miR-199a-5p/XIAP interaction across species, providing a rationale to investigate its functional behaviour in human ovarian cancer models.

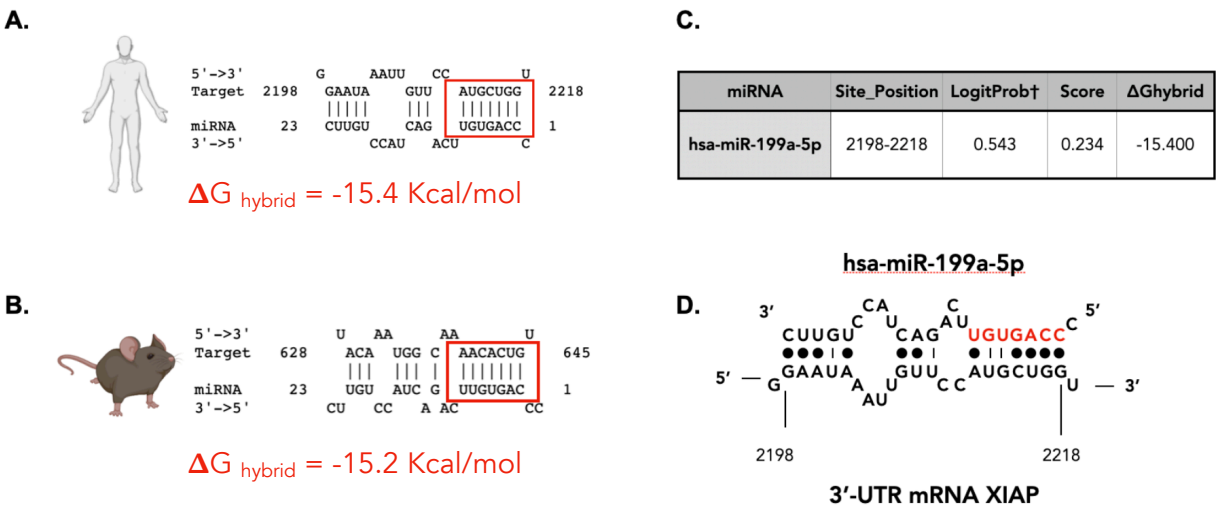

miRNA	Site_Position	LogitProb†	Score	ΔGhybrid
hsa-miR-199a-5p	2198-2218	0.543	0.234	-15.400

Figure 1. Cross-species computational support for conserved miR-199a-5p binding to the XIAP 3′UTR.
(A) Predicted duplex formed between hsa-miR-199a-5p and the human XIAP 3′ untranslated region (3′UTR; positions 2198–2218), showing canonical seed pairing and extended base complementarity. (B) Predicted conserved interaction between miR-199a-5p and the murine XIAP orthologue (positions 628–645), also showing canonical seed pairing and comparable hybridisation energy (ΔG_hybrid = −15.2 kcal/mol). (C) Summary of STarMir predictions for the human XIAP target site. Site_Position indicates the nucleotide coordinates of the predicted binding region within the human XIAP 3′UTR. LogitProb represents the probability of a functional miRNA-binding site, as estimated by a logistic regression model trained on CLIP-derived datasets; values >0.5 were considered supportive of binding. Score integrates multiple determinants of interaction, including seed pairing, 3′ pairing, target accessibility, AU-rich flanking context and hybridisation energy. More negative ΔG_hybrid values indicate greater thermodynamic stability of duplex formation. (D) RNA secondary structure model of the human XIAP 3′UTR surrounding the predicted miR-199a-5p binding site, generated using RNAfold. The predicted miRNA-binding region is highlighted, and dots indicate base-pairing interactions within the local RNA structure.

Basal expression of the miR-199a-5p/XIAP axis in cisplatin-sensitive and cisplatin-resistant ovarian cancer cells

To investigate whether basal differences in the miR-199a-5p/XIAP axis were associated with the resistant phenotype, we compared transcript and protein expression in cisplatin-sensitive A2780 cells and their cisplatin-resistant derivative A2780cis.

Differential expression of miR-199a-5p and XIAP in cisplatin-resistant cells

TaqMan-based RT–qPCR analysis revealed a significant downregulation of miR-199a-5p in A2780cis cells relative to A2780 (fold change −2.58; $t_4 = 3.46$, $p = 0.013$; $n = 3$; Fig. 2A, upper panel). In contrast, XIAP mRNA levels did not differ significantly between the two cell lines ($t_4 = 1.106$, $p = 0.165$; $n = 3$; Fig. 2A, lower panel), indicating that the resistant phenotype was associated with reduced basal miR-199a-5p expression without a corresponding change in XIAP transcript abundance.

Basal XIAP protein expression in ovarian cancer cell lines

To determine whether this difference was reflected at protein level, XIAP expression was examined by western blot in whole-cell lysates from three independent matched experiments. A2780cis cells showed slightly higher XIAP protein levels than A2780 cells (1.52 ± 0.41 vs. 1.27 ± 0.31), but this difference did not reach statistical significance ($t_2 = 1.709$, $p = 0.11$; one-tailed paired t-test; 95% CI: −0.861 to 0.3; Fig. 2B). Thus, under basal conditions, XIAP protein abundance was not significantly altered in the resistant line despite the marked reduction in miR-199a-5p.

Single-cell-level analysis of miR-199a-5p and XIAP by FISH and immunofluorescence

To assess whether cell-associated fluorescence measurements reproduced the pattern observed in bulk assays, combined fluorescence in situ hybridisation (FISH) for miR-199a-5p and immunofluorescence for XIAP were performed across three independent experiments (Fig. 2C). Quantitative image analysis showed that XIAP-associated fluorescence intensity was moderately higher in A2780cis cells (102.8 ± 44.0) than in A2780 cells (91.2 ± 27.3), although this difference was not statistically significant ($p = 0.209$; Mann–Whitney U test). In contrast, miR-199a-5p-associated fluorescence intensity was significantly reduced in A2780cis cells (41.2 ± 21.7 a.u.) relative to A2780 cells (60.5 ± 27.9 a.u.; $p = 0.009$). These single-cell-level measurements were therefore consistent with the basal expression pattern detected by RT–qPCR and immunoblotting, supporting reduced miR-199a-5p expression in the resistant phenotype without a significant basal increase in XIAP.

A.

	ΔCt	T-test			fold decrease	
		mean diff (ΔΔCt)		p value		
A2780	3.89 ± 0.41	A2780 vs. A2780 cis	2.55 (0.27, 2.41)	$T_4 = 3.46$	5.85	(0.83 , 10.63)
A2780 cis	6.44 ± 2.11			**p = 0.013 (*)**		

	ΔCt	T-test			fold increase	
		mean diff (ΔΔCt)		p value		
A2780	13.001 ± 0.63	A2780 vs. A2780 cis	-0.472 (-1.656 , 0.712)	$T_4 = 1.106$	1.387	(0.61 , 3.151)
A2780 cis	12.53 ± 0.232			p = 0.165		

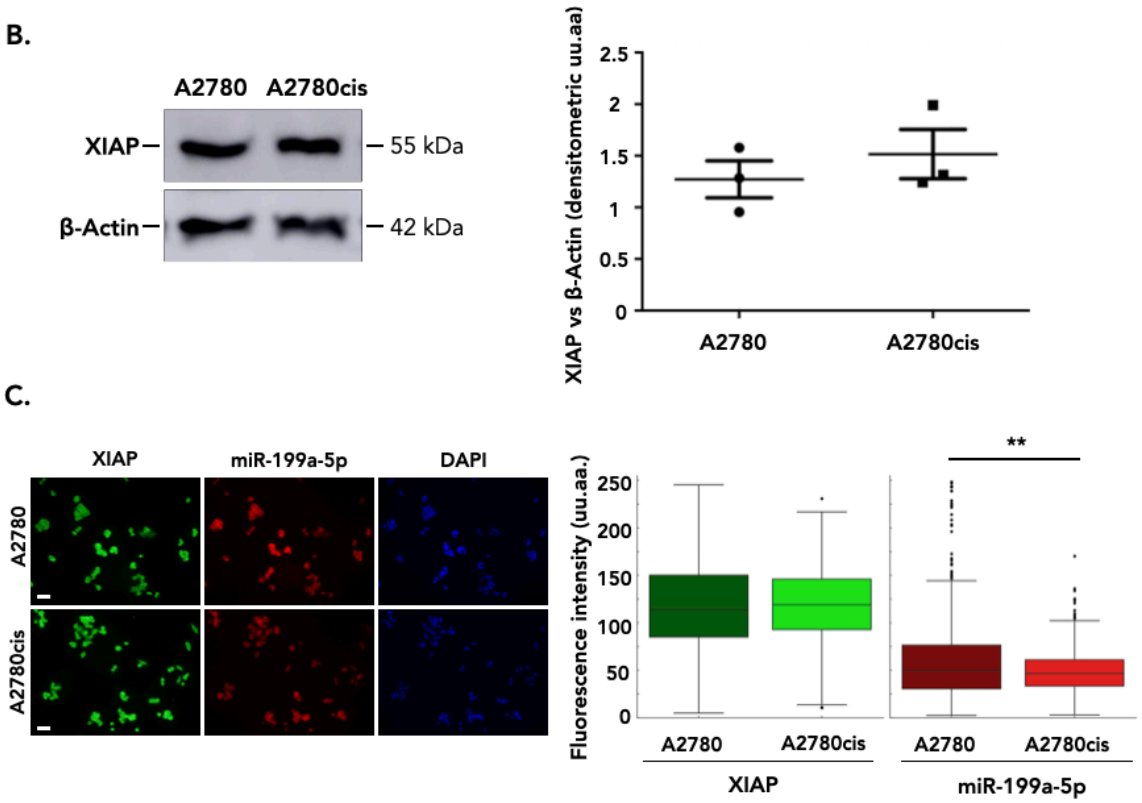

Figure 2. Basal expression of miR-199a-5p and XIAP in cisplatin-sensitive (A2780) and cisplatin-resistant (A2780cis) ovarian cancer cells. (A) RT–qPCR analysis of basal miR-199a-5p (upper panel) and XIAP mRNA (lower panel) expression in A2780 and A2780cis cells. Data are shown as ΔCt values, mean differences (ΔΔCt), p values and fold change estimates from Student's t-tests. (B) Representative immunoblot showing basal XIAP and β-actin expression in A2780 and A2780cis cells (left), and densitometric quantification of XIAP normalised to β-actin (right). Data represent mean ± SEM from three independent experiments. (C) Combined fluorescence in situ hybridisation (FISH) for miR-199a-5p (red) and immunofluorescence for XIAP (green) in A2780 (upper panel) and A2780cis (lower panel) cells, with nuclei counterstained with DAPI (blue). Boxplots show per-cell fluorescence intensity distributions for each marker. Statistical analysis was performed using Mann–Whitney U tests. ** $p < 0.01$. Scale bar, 50 μm.

Differential regulation of XIAP by miR-199a-5p under basal conditions

To determine whether miR-199a-5p modulated XIAP expression under untreated conditions, basal XIAP protein levels were analysed after miR-199a-5p transfection in cisplatin-sensitive (A2780) and cisplatin-resistant (A2780cis) ovarian cancer cells (Fig. 3A). In A2780 cells, miR-199a-5p transfection significantly reduced XIAP protein levels

compared with the negative control (one-tailed paired t-test, p = 0.0359, n = 6; Fig. 3B, left). In contrast, no significant reduction in XIAP expression was detected in A2780cis cells following miR-199a-5p transfection (p = 0.0765, n = 5; Fig. 3B, right). These findings indicate that basal XIAP repression by miR-199a-5p was evident in cisplatin-sensitive cells but attenuated in the resistant phenotype.

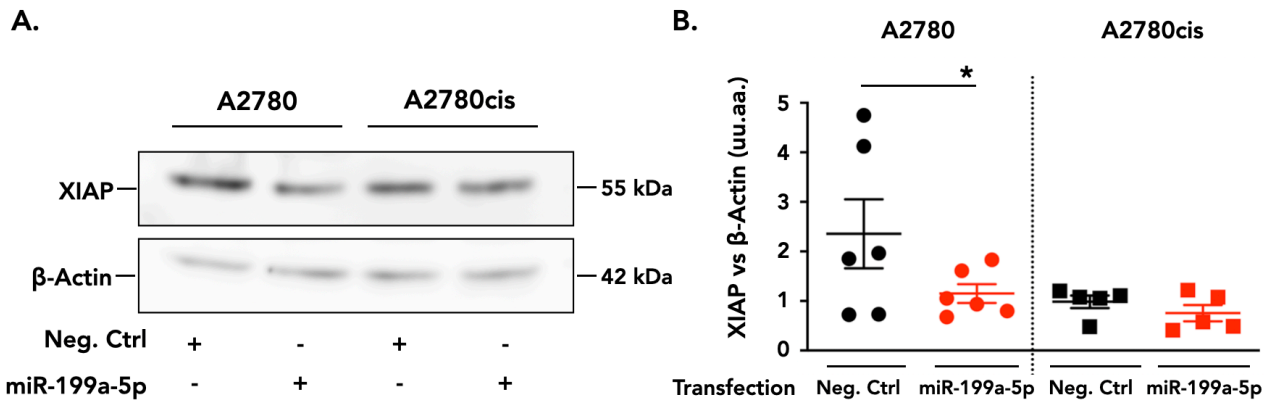

Figure 3. Effect of miR-199a-5p transfection on basal XIAP protein expression in A2780 and A2780cis ovarian cancer cells. (A) Representative Western blot of XIAP in whole-cell lysates from A2780 (left) and A2780cis (right) cells transfected with either a negative control mimic or miR-199a-5p mimic under basal conditions. β-Actin was used as a loading control. (B) Densitometric quantification of XIAP normalised to β-actin from six independent experiments in A2780 cells (circles) and five independent experiments in A2780cis cells (squares). Statistical analysis was performed using one-tailed paired t-tests. $p < 0.05$.

Effect of miR-199a-5p on cisplatin response in ovarian cancer cells

To examine whether miR-199a-5p modulates cisplatin response, we assessed cell viability, membrane integrity, apoptotic activity and XIAP protein levels in cisplatin-sensitive (A2780) and cisplatin-resistant (A2780cis) ovarian cancer cells.

Validation of the cisplatin-resistant phenotype

To confirm the resistant phenotype of A2780cis cells, MTT assays were used to compare cisplatin sensitivity between A2780cis and parental A2780 cells. A2780cis cells exhibited a higher EC_{50} than A2780 cells (44.56 μM vs. 12.16 μM; Fig. 4), consistent with reduced cisplatin sensitivity in the resistant line.

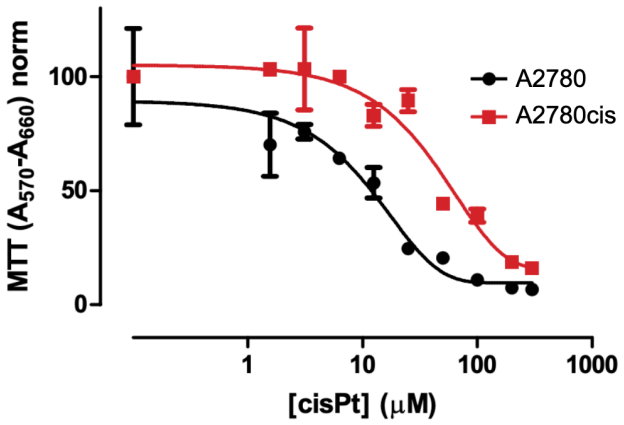

Figure 4. Cisplatin sensitivity of A2780 and A2780cis ovarian cancer cells.
Dose–response curves were generated from MTT assays following 72 h exposure to increasing concentrations of cisplatin. EC_{50} values were calculated to compare cisplatin sensitivity between the two cell lines. Data represent mean ± SEM from three independent experiments performed in triplicate.

Distinct effects of miR-199a-5p on cisplatin response in sensitive and resistant ovarian cancer cells

To evaluate the impact of miR-199a-5p on cisplatin sensitivity, cell viability was assessed in A2780 and A2780cis ovarian cancer cells using the MTT assay following transfection with either miR-199a-5p or a negative control, in the presence or absence of cisplatin (Fig. 5).

In A2780 cells (Fig. 5, left), the linear mixed-effects model without interaction revealed significant main effects of cisplatin treatment ($F(1,7) = 15.30$, $p = 0.0058$) and miR-199a-5p transfection ($F(1,7) = 10.66$, $p = 0.0138$) on cell viability. Cisplatin alone reduced viability by 13.9% relative to untreated controls (0.4213 ± 0.0343 vs. 0.4891 ± 0.0307; $p = 0.0234$), whereas miR-199a-5p alone produced a smaller reduction, with a trend towards decreased viability that did not reach statistical significance (0.4357 ± 0.0213 vs. 0.4891 ± 0.0307; $p = 0.0531$). Under combined treatment, viability was reduced by 32.7% relative to untreated controls (0.3294 ± 0.0389 vs. 0.4891 ± 0.0307; $p = 0.0061$). This decrease was numerically consistent with the summed effects of each individual treatment, supporting an additive interpretation rather than evidence of interaction.

In contrast, neither miR-199a-5p transfection nor cisplatin treatment significantly altered viability in A2780cis cells (Fig. 5, right). The model detected no main effect of miR-199a-5p ($F(1,7) = 0.44$, $p = 0.530$) or cisplatin ($F(1,7) = 3.40$, $p = 0.108$), and the combined treatment did not significantly reduce viability compared with untreated controls or single-treatment conditions (Tukey-adjusted $p = 0.7343$). These results indicate that miR-199a-5p enhanced cisplatin-associated loss of viability in sensitive cells, whereas this effect was not observed in the resistant line.

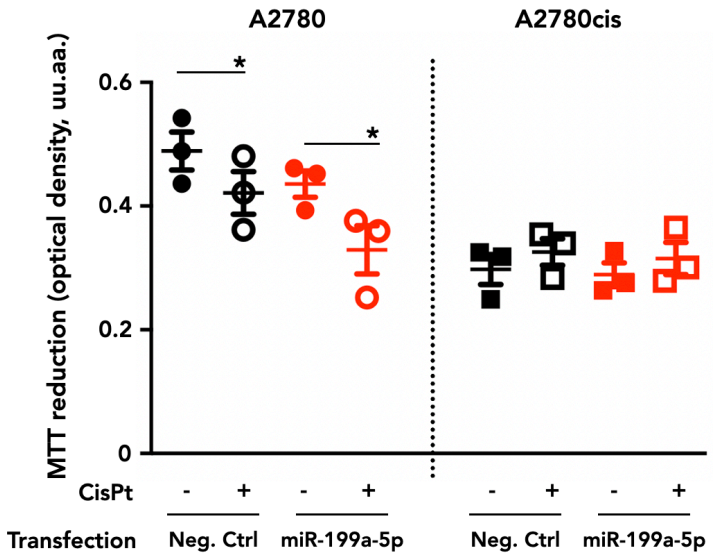

Figure 5. Effect of miR-199a-5p and cisplatin on cell viability in A2780 and A2780cis cells. A2780 (circles) and A2780cis (squares) ovarian cancer cells were transfected with either a negative control mimic (NC) or a miR-199a-5p mimic, and subsequently treated with or without 12.5 μM cisplatin (cisPt) for 24 h. Cell viability was assessed by MTT assay and expressed as optical density (OD_{570}–OD_{660}). Each point represents one independent experiment (n = 3), and bars indicate mean ± SEM. Filled symbols indicate untreated conditions (cisPt−), and open symbols indicate cisplatin-treated conditions (cisPt+). Statistical analysis was performed using a linear mixed-effects model followed by Tukey-adjusted post hoc comparisons. *$p < 0.05$.

Propidium iodide staining reveals enhanced cell death with combined treatment

PI staining assays were performed in A2780 (Fig. 6A) and A2780cis cells (Fig. 6B)

transfected with either a miR-199a-5p mimic or a negative control, followed by treatment with 12.5 μM cisplatin for 24 h.

In A2780 cells (Fig. 6C, left), miR-199a-5p significantly increased PI positivity ($F(1,9) = 7.6558$, $p = 0.0219$), and a significant interaction with cisplatin was detected ($F(1,9) = 6.7081$, $p = 0.0292$), whereas cisplatin alone had no significant main effect ($F(1,9) = 2.5721$, $p = 0.1432$). Post hoc analysis showed that the combined treatment significantly increased the proportion of PI-positive cells compared with cisplatin alone ($t(9) = -3.788$, $p = 0.0185$). Comparisons with untreated controls ($t(9) = -3.091$, $p = 0.0524$) and with miR-199a-5p alone ($t(9) = -2.965$, $p = 0.0633$) showed non-significant trends towards increased PI positivity. No significant differences were detected between untreated controls and either single treatment, or between the two single-treatment conditions.

In contrast, in A2780cis cells (Fig. 6C, right), no significant effects of miR-199a-5p ($F(1,9) = 0.1223$, $p = 0.7346$), cisplatin ($F(1,9) = 4.0582$, $p = 0.0748$), or their interaction ($F(1,9) = 3.0564$, $p = 0.1144$) were detected, indicating that PI incorporation remained largely unchanged across conditions. Together, these findings indicate that miR-199a-5p enhanced cisplatin-associated late cell death in sensitive cells, whereas this effect was not evident in the resistant line.

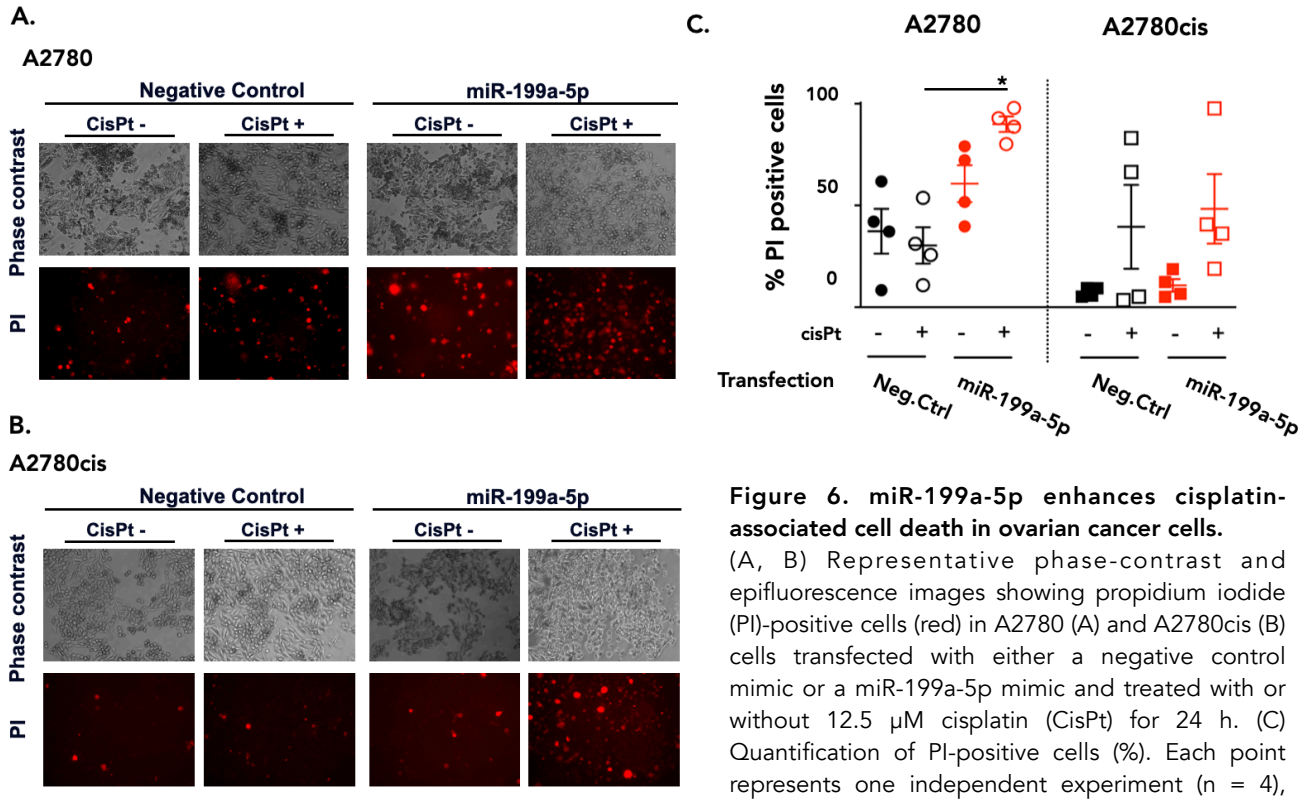

Figure 6. miR-199a-5p enhances cisplatin-associated cell death in ovarian cancer cells. (A, B) Representative phase-contrast and epifluorescence images showing propidium iodide (PI)-positive cells (red) in A2780 (A) and A2780cis (B) cells transfected with either a negative control mimic or a miR-199a-5p mimic and treated with or without 12.5 μM cisplatin (CisPt) for 24 h. (C) Quantification of PI-positive cells (%). Each point represents one independent experiment (n = 4), and bars indicate mean ± SEM. Statistical analysis was performed using a linear mixed-effects model with transfection, cisplatin treatment and their interaction as fixed effects, and experimental day as a random intercept, followed by Tukey-adjusted post hoc comparisons. *$p < 0.05$.

miR-199a-5p increases pro-apoptotic activation in response to cisplatin in ovarian cancer cells

To assess the pro-apoptotic effects of miR-199a-5p in the context of cisplatin treatment, caspase-3/7 activity was quantified by fluorescence microscopy in A2780 and A2780cis ovarian cancer cell lines following transfection with miR-199a-5p or a negative control, and treatment with or without 12.5 μM cisplatin for 24 h.

In the cisplatin-sensitive A2780 line (Fig. 7A, upper panel; Fig. 7B, left), cisplatin significantly increased the proportion of caspase-positive cells ($F(1,12) = 27.8896$, $p = 0.00019$), whereas miR-199a-5p transfection ($F(1,12) = 3.2912$, $p = 0.0947$) and the interaction between both factors ($F(1,12) = 0.6172$, $p = 0.4473$) were not significant. Post hoc analysis confirmed that cisplatin increased caspase-3/7 activity relative to untreated controls in both negative control-transfected cells ($t(9) = -3.179$, $p = 0.0459$) and miR-199a-5p-transfected cells ($t(9) = -4.290$, $p = 0.0090$), whereas no significant differences were detected between transfection conditions either in the absence or presence of cisplatin. These results indicate that, in A2780 cells, caspase-3/7 activation was primarily driven by cisplatin treatment.

In contrast, in A2780cis cells (Fig. 7A, lower panel; Fig. 7B, right), cisplatin ($F(1,9) = 11.4521$, $p = 0.0081$), miR-199a-5p transfection ($F(1,9) = 25.5065$, $p = 0.00069$), and their interaction ($F(1,9) = 6.9905$, $p = 0.0267$) all showed significant effects, indicating that caspase-3/7 activation depended on treatment context. Post hoc analysis showed that, under cisplatin exposure, miR-199a-5p transfection significantly increased caspase-3/7 activity compared with negative control-transfected cells ($t(9) = -5.441$, $p = 0.0019$), and that cisplatin significantly increased caspase activity in miR-199a-5p-transfected cells ($t(9) = -4.262$, $p = 0.0093$). By contrast, no transfection-related differences were observed in the absence of cisplatin, and cisplatin alone did not differ significantly from untreated controls in negative control-transfected cells. Together, these findings indicate that miR-199a-5p enhanced cisplatin-associated caspase-3/7 activation in the resistant line, whereas in sensitive cells caspase activation was largely attributable to cisplatin itself.

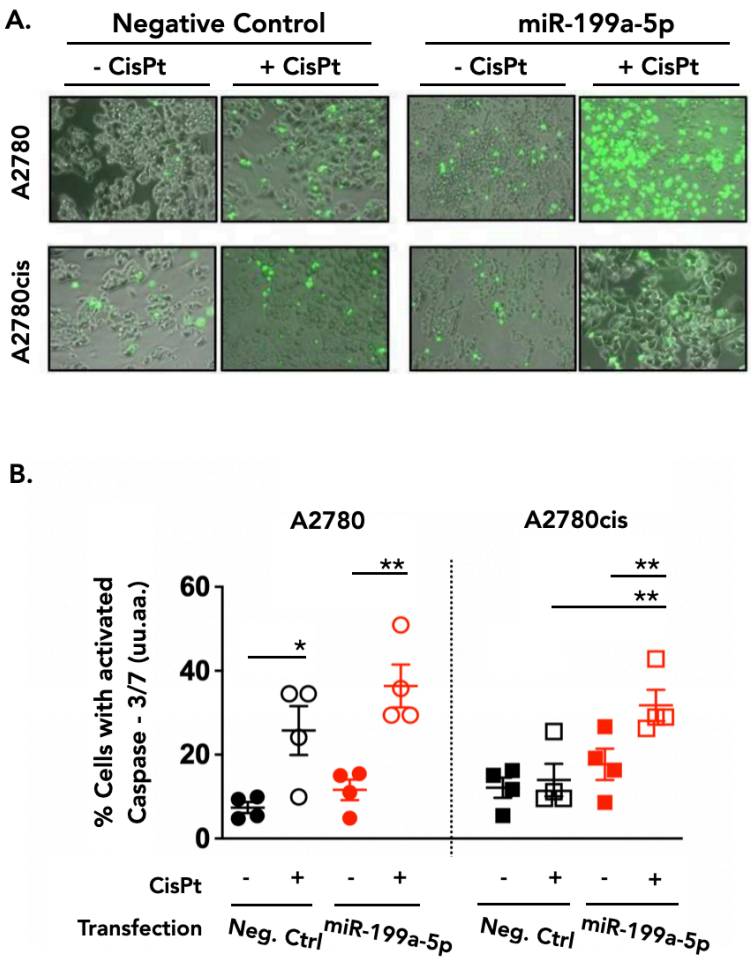

Figure 7. miR-199a-5p enhances cisplatin-associated caspase-3/7 activation in ovarian cancer cells. (A) Representative fluorescence microscopy images showing caspase-3/7-positive cells (green) in A2780 and A2780cis ovarian cancer cells transfected with either a negative control mimic or a miR-199a-5p mimic, and treated with or without 12.5 μM cisplatin (CisPt) for 24 h. (B) Quantification of caspase-3/7-positive cells (%). A2780 cells are shown on the left (circles) and A2780cis cells on the right (squares). Each point represents one independent experiment (n = 4), and bars indicate mean ± SD. Statistical analysis was performed using a linear mixed-effects model with transfection, cisplatin treatment and their interaction as fixed effects, and experimental day as a random intercept, followed by Tukey-adjusted post hoc comparisons. *p < 0.05, **p < 0.01.

Caspase-3 activation in response to miR-199a-5p and cisplatin in ovarian cancer cells

To assess whether miR-199a-5p modulates caspase-dependent apoptotic signalling, cleaved caspase-3 levels were analysed by western blot in whole-cell lysates from A2780 (Fig. 8A) and A2780cis cells (Fig. 8B), followed by densitometric quantification normalised to loading controls.

In A2780 cells, cisplatin significantly increased cleaved caspase-3 levels ($F(1,9) = 25.28$, $p = 0.0007$), whereas miR-199a-5p transfection ($F(1,9) = 0.008$, $p = 0.931$) and the interaction between both factors ($F(1,9) = 2.76$, $p = 0.131$) were not significant. Post hoc analysis showed that, in control-transfected cells, cisplatin induced a marked increase in cleaved caspase-3 relative to untreated controls (estimated difference = 1.201 ± 0.239, $p = 0.0032$). A similar increase was observed in miR-199a-5p-transfected cells, although this effect did not remain significant after multiple testing correction (estimated difference = 0.640 ± 0.239, $p = 0.0973$) (Fig. 8C, left).

In contrast, in A2780cis cells, no statistically significant effects of cisplatin ($F(1,8) = 4.77$, $p = 0.0605$), miR-199a-5p transfection ($F(1,8) = 2.28$, $p = 0.1697$), or their interaction ($F(1,8) = 0.67$, $p = 0.4378$) were detected (Fig. 8C, right), although a non-significant trend towards increased caspase-3 activation was observed in response to cisplatin. Together, these results indicate that cleaved caspase-3 accumulation was primarily driven by cisplatin in sensitive cells, whereas resistant cells did not show a comparable apoptotic response under these conditions.

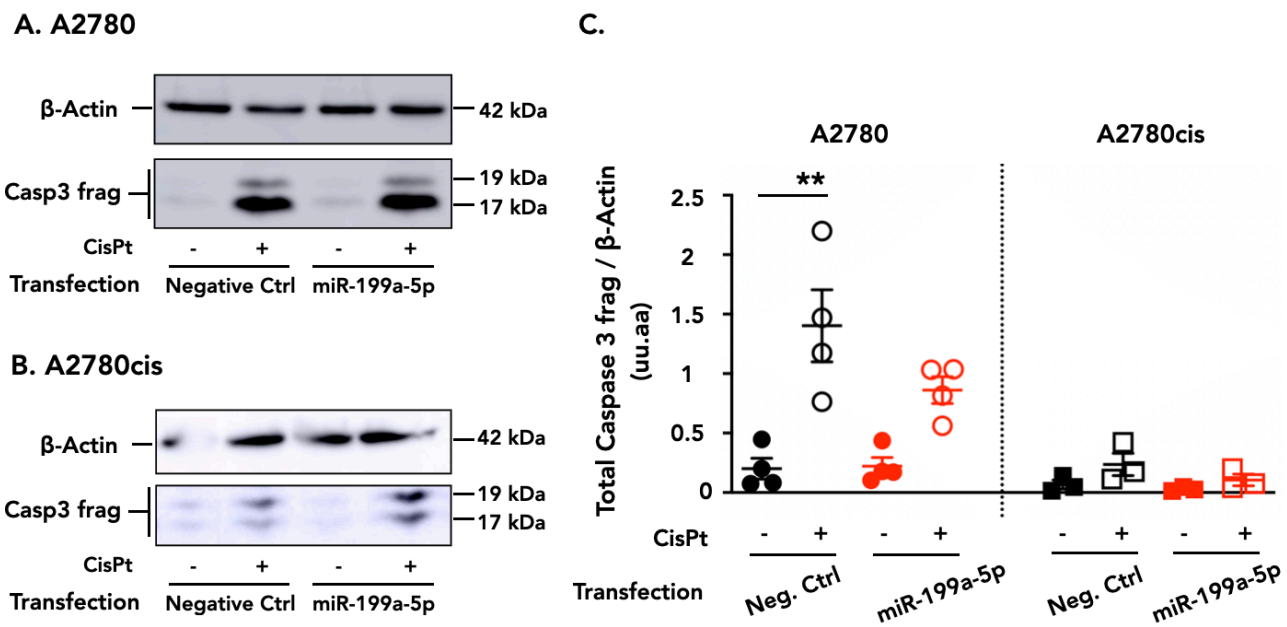

Figure 8. Effects of cisplatin and miR-199a-5p on cleaved caspase-3 levels in ovarian cancer cells. (A, B) Representative western blot analysis of cleaved caspase-3 (Casp3 frag) in whole-cell lysates from A2780 (A) and A2780cis (B) ovarian cancer cells transfected with either a negative control mimic or a miR-199a-5p mimic, and treated with or without cisplatin (CisPt; 12.5 μM, 24 h). β-Actin was used as a loading control. (C) Densitometric quantification of cleaved caspase-3 normalised to β-actin. A2780 cells are shown on the left (circles; n = 4) and A2780cis cells on the right (squares; n = 3). Each point represents one independent experiment, and bars indicate mean ± SEM. Statistical analysis was performed using a linear mixed-effects model with transfection, cisplatin treatment and their interaction as fixed effects, and experimental day as a random intercept, followed by Tukey-adjusted post hoc comparisons. **$p < 0.01$.

Differential regulation of XIAP by miR-199a-5p and cisplatin

To evaluate the regulation of XIAP by miR-199a-5p under cisplatin exposure, western blot analyses were performed in A2780 (Fig. 9A, left) and A2780cis cells (Fig. 9A, right) transfected with a miR-199a-5p mimic or a negative control and treated with or without 12.5 μM cisplatin. XIAP protein levels were quantified by densitometry and normalised to β-actin.

In A2780 cells (Fig. 9B, left), cisplatin significantly reduced XIAP levels ($F(1,9) = 9.3062$, $p = 0.0138$), whereas miR-199a-5p transfection was not significant ($F(1,9) = 1.9051$, $p = 0.2008$) and the interaction showed a non-significant trend ($F(1,9) = 3.9819$, $p = 0.0771$). In agreement with the basal analysis shown in Fig. 3, miR-199a-5p significantly reduced XIAP under untreated conditions ($t(9) = -2.387$, $p = 0.0408$). Post hoc analysis further showed that cisplatin reduced XIAP in negative control-transfected cells ($t(9) = 3.568$, $p = 0.0257$), whereas no additional reduction was detected in miR-199a-5p-transfected cells ($t(9) = 0.746$, $p = 0.8761$). No significant differences between transfection conditions were detected either in the absence or presence of cisplatin.

In contrast, in A2780cis cells (Fig. 9B, right), a significant interaction between miR-199a-5p transfection and cisplatin treatment was observed ($F(1,9) = 12.9292$, $p = 0.0058$), whereas neither miR-199a-5p ($F(1,9) = 2.7892$, $p = 0.1292$) nor cisplatin alone ($F(1,9) = 0.8596$, $p = 0.3780$) showed significant main effects. Post hoc analysis showed that cisplatin reduced XIAP in negative control-transfected cells ($t(9) = 3.198$, $p = 0.0446$), whereas the combined miR-199a-5p + cisplatin condition did not differ from untreated

controls (t(9) = −0.525, p = 0.9508). Notably, under cisplatin treatment, XIAP levels were significantly higher in miR-199a-5p-transfected cells than in negative control-transfected cells (t(9) = −3.723, p = 0.0203), whereas no transfection-related differences were observed in the absence of cisplatin. Together, these results show that XIAP regulation by miR-199a-5p differed markedly between sensitive and resistant cells under cisplatin exposure.

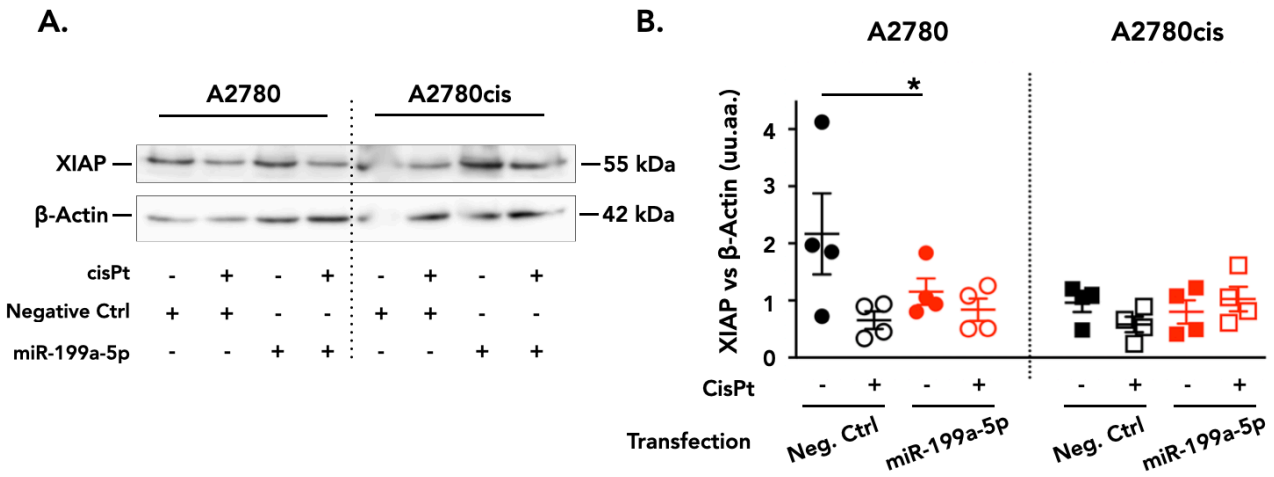

Figure 9. Effects of cisplatin and miR-199a-5p on XIAP protein levels in ovarian cancer cells.
(A) Representative western blot analysis of XIAP in whole-cell lysates from A2780 (left) and A2780cis (right) ovarian cancer cells transfected with either a negative control mimic or a miR-199a-5p mimic, and treated with or without cisplatin (CisPt; 12.5 μM, 24 h). β-Actin was used as a loading control. (B) Densitometric quantification of XIAP normalised to β-actin. A2780 cells are shown on the left (circles) and A2780cis cells on the right (squares). Each point represents one independent experiment (n = 4), and bars indicate mean ± SEM. Statistical analysis was performed using a linear mixed-effects model with transfection, cisplatin treatment and their interaction as fixed effects, and experimental day as a random intercept, followed by Tukey-adjusted post hoc comparisons. *p < 0.05.

Taken together, these in vitro findings indicate that miR-199a-5p influences cisplatin response differently in sensitive and resistant ovarian cancer cells. In A2780 cells, miR-199a-5p was associated with reduced basal XIAP expression and with enhanced cisplatin-associated loss of viability and apoptotic activation. In A2780cis cells, however, this relationship was reconfigured, with treatment-dependent effects on caspase activation and XIAP regulation that were not matched by a comparable reduction in overall viability.

Spatial and subcellular co-localization of miR-199a-5p and XIAP in human ovarian tissue and HGSOC

To characterise the spatial and subcellular distribution of miR-199a-5p and XIAP in human ovarian tissue, multiplex fluorescence in situ hybridisation (FISH) combined with immunofluorescence (IF) was performed on FFPE sections from non-neoplastic ovaries and high-grade serous ovarian carcinoma (HGSOC) samples. At low magnification (10×; Fig. 10A), non-neoplastic ovarian tissue displayed intense XIAP staining predominantly localised within glandular epithelial structures, whereas miR-199a-5p signal was weak and largely confined to stromal regions. In contrast, HGSOC samples exhibited strong and widespread miR-199a-5p signal across both epithelial and stromal compartments,

whereas XIAP remained detectable but showed a more heterogeneous distribution (Fig. 10B).

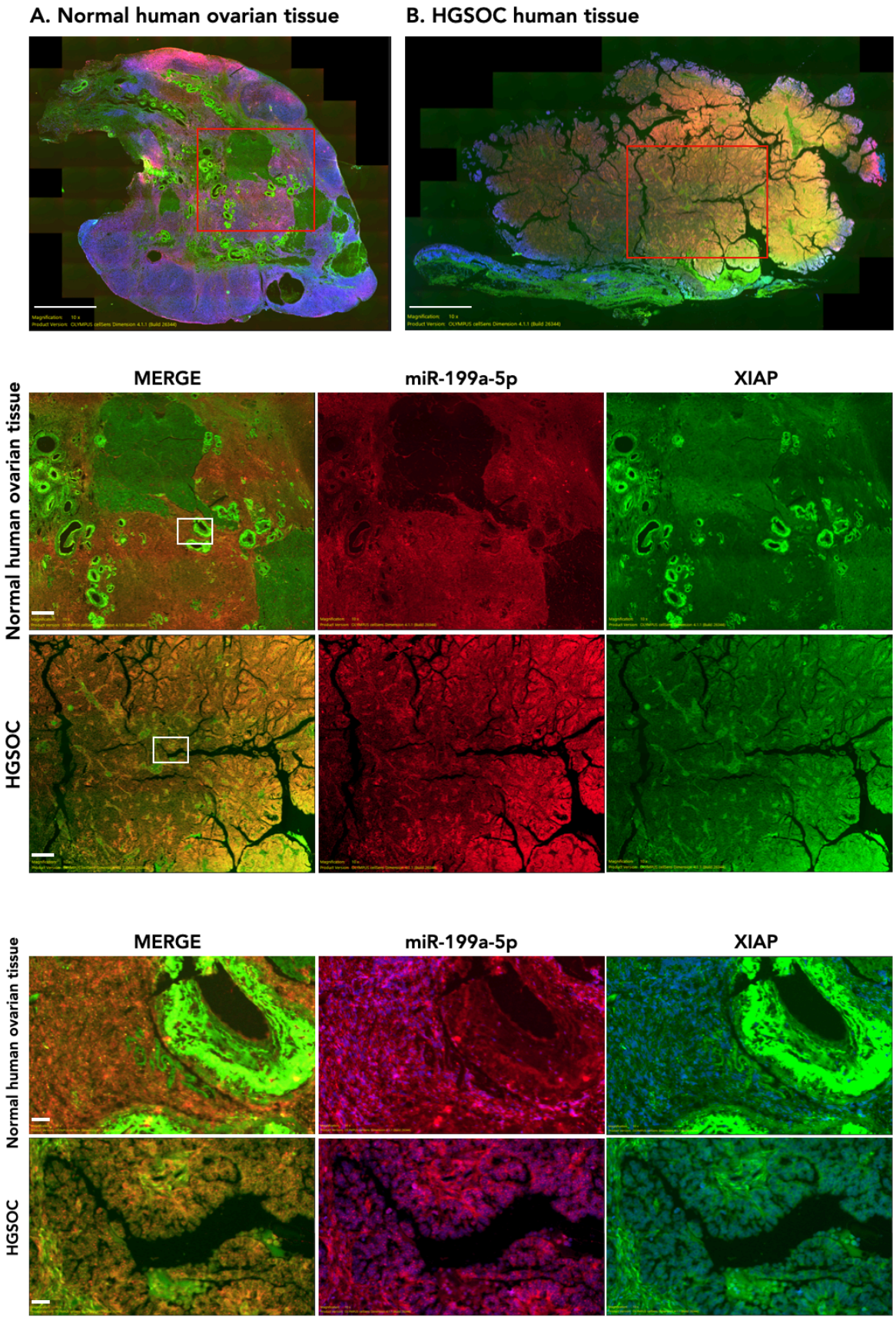

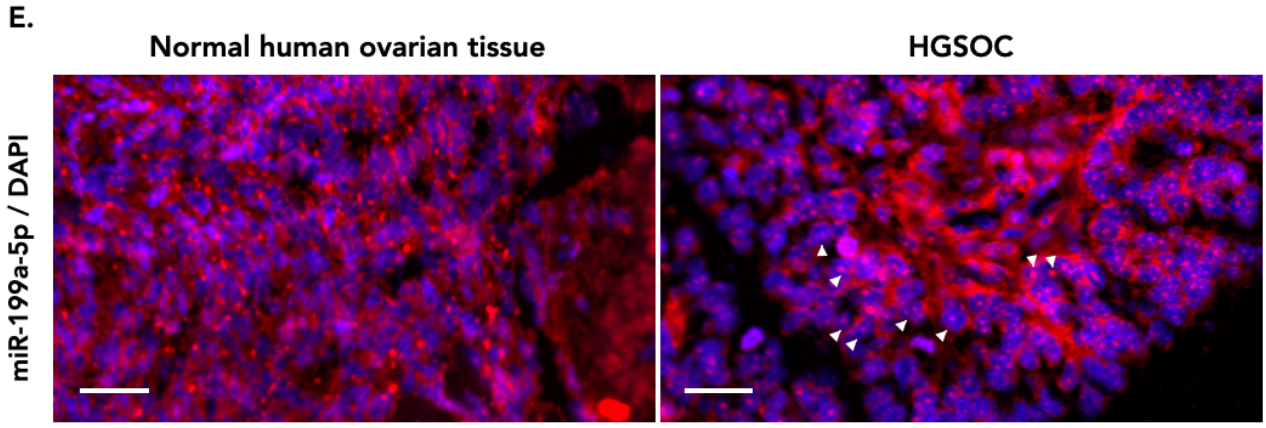

Figure 10. Spatial and subcellular localisation of miR-199a-5p and XIAP in non-neoplastic ovary and HGSOC. Representative multiplex fluorescence in situ hybridisation (FISH) and immunofluorescence (IF) images of formalin-fixed paraffin-embedded (FFPE) sections from non-neoplastic human ovarian tissue and high-grade serous ovarian carcinoma (HGSOC). (A, B) Low-magnification overview images of non-neoplastic ovary (A) and HGSOC (B) showing miR-199a-5p (red), XIAP (green) and nuclei (DAPI, blue). Red boxes indicate regions selected for higher-magnification analysis. (C, D) Intermediate- (C) and high-magnification (D) views of the selected regions. For each condition, panels show merged signal (left), miR-199a-5p/DAPI (middle) and XIAP/DAPI (right). (E) Digitally enlarged views of the high-magnification fields shown in (D), highlighting the subcellular distribution of miR-199a-5p in non-neoplastic ovary (left) and HGSOC (right). Arrows indicate cells showing nuclear-associated signal. Scale bars, 100 µm in (A, B), 50 µm in (C, D), and 20 µm in (E).

At intermediate magnification (Fig. 10C), XIAP localisation in control tissue remained restricted to epithelial territories, with minimal overlap with miR-199a-5p, which was largely excluded from these regions (Fig. 10C, upper panel). In tumour tissue, by contrast, both signals were detected within overlapping cellular domains, producing merged fluorescence consistent with partial spatial overlap (Fig. 10C, lower panel). High-magnification imaging further showed that in non-neoplastic ovary, XIAP was predominantly cytoplasmic in epithelial cells, whereas miR-199a-5p remained faint and peripherally distributed (Fig. 10D, left). In HGSOC cells, miR-199a-5p displayed strong cytoplasmic and prominent perinuclear—and occasionally nuclear—localisation, a pattern not observed in control tissue (Fig. 10D, right). Nuclear-associated signal was also observed at higher magnification in numerous tumour cells (Fig. 10E).

Quantitative colocalisation analysis of miR-199a-5p and XIAP in human ovarian tissue

Quantitative colocalisation analysis identified selective differences between non-neoplastic and tumour ovarian tissues (Table 3). To minimise selection bias and ensure representative sampling of the tissue section, ten spatially distributed ROIs were defined per sample, and ROI-level measurements were aggregated to a single value per image before statistical analysis. Between-group comparisons were then performed at the patient level (n = 10 controls, n = 9 tumours).

Table 3. Intensity-dependent descriptors K1 and K2 further distinguished tumor from control tissues.

Variable	Control	Tumor	Test	p_value
Pearson	0.464 ± 0.114	0.541 ± 0.142	Welch t-test	0.214901
M1	0.493 ± 0.062	0.574 ± 0.137	Mann–Whitney U	**0.022018**
M2	0.510 ± 0.141	0.566 ± 0.191	Welch t-test	0.489253
Overlap coefficient	0.933 ± 0.035	0.926 ± 0.025		
CCF_MAX	0.456 ± 0.115	0.534 ± 0.141	Welch t-test	0.211654
CCF_MIN	0.296 ± 0.101	0.371 ± 0.130	Welch t-test	0.181979
K1	0.484 (median)	1.677 (median)	Mann–Whitney U	**0.000022**
K2	1.822 (median)	0.512 (median)	Mann–Whitney U	**0.000100**
FWHM	20.506 (median)	20.235 (median)	Mann–Whitney U	0.660720

Pearson's correlation coefficient showed a modest increase in tumour samples (0.541 ± 0.142) relative to controls (0.464 ± 0.114), although this difference was not significant ($p = 0.2149$). Manders' M1 was significantly higher in tumours than in controls (0.574 ± 0.137 vs. 0.493 ± 0.062; $p = 0.0220$), whereas M2 did not differ significantly between groups (0.566 ± 0.191 vs. 0.510 ± 0.141; $p = 0.4893$). The overlap coefficient remained similarly high in both groups (0.926 ± 0.025 in tumour tissue vs. 0.933 ± 0.035 in control tissue).

Intensity-weighted descriptors (K1 and K2), reported as medians according to their original definition, further separated the two tissue types. Control samples showed lower K1 and higher K2 values, whereas tumour samples displayed the opposite pattern, with significantly increased K1 (median 1.677 vs. 0.484; $p = 0.000022$) and reduced K2 (median 0.512 vs. 1.822; $p = 0.000100$). Among the metrics analysed, M1 and K1 showed the most prominent differences between non-neoplastic and tumour tissues. Together, these findings identify a tumour-associated spatial reorganisation of the miR-199a-5p/XIAP axis in human HGSOC, accompanied by altered subcellular distribution of miR-199a-5p.

Taken together, the human tissue data extend the in vitro findings by showing that the miR-199a-5p/XIAP axis is not only functionally reconfigured across cisplatin-sensitive and cisplatin-resistant cellular states, but also spatially reorganised in human HGSOC. Whereas the cell-based models revealed context-dependent differences in the relationship between miR-199a-5p, XIAP and apoptotic output, tissue-level analysis identified a tumour-associated redistribution of both signals, increased spatial overlap, and an altered subcellular pattern of miR-199a-5p. These findings support the view that regulation of the miR-199a-5p/XIAP axis depends not only on treatment response state but also on spatial and subcellular context within the tumour.

DISCUSSION

Ovarian cancer remains a leading cause of gynaecological cancer-related mortality, largely because of late-stage diagnosis and the development of resistance to platinum-based chemotherapy [20,21]. Impaired apoptotic execution is a central feature of this resistant phenotype, and altered regulation of inhibitor of apoptosis proteins, including XIAP, has been implicated in reduced chemotherapy-induced cell death [22]. In parallel, deregulated miRNA expression has been widely linked to ovarian cancer progression and therapeutic response, consistent with the ability of miRNAs to regulate survival, stress-response and apoptotic pathways [8,23]. Within this context, miR-199a-5p has been associated with tumour-suppressive functions and with chemotherapy response in ovarian cancer [24,25].

Our laboratory previously identified XIAP as a direct target of miR-199a-5p13, providing a mechanistic basis for examining this axis in ovarian cancer models. In the present study, STarMir and RNAfold analyses supported the presence of an accessible and energetically favourable miR-199a-5p binding site within the XIAP 3'UTR, conserved across species, in line with broader evidence that mammalian miRNA target sites are frequently evolutionarily maintained [26]. This is also consistent with established models showing that local RNA structure and target-site accessibility influence the efficiency of miRNA-mediated repression [14,27]. The relevance of the present study therefore lies not in re-establishing the identity of the target, but in defining how the functional behaviour of this interaction changes across cellular states and treatment conditions.

At baseline, the resistant A2780cis phenotype was characterised by reduced miR-199a-5p levels without significant changes in XIAP mRNA, indicating altered post-transcriptional balance rather than transcriptional upregulation of XIAP. This decrease in miR-199a-5p was also reproduced by cell-associated fluorescence analysis, supporting the consistency of the basal shift across analytical levels. These findings are in keeping with previous reports linking the miR-199 family to platinum response in ovarian cancer, including studies associating loss of miR-199-related regulation with acquired resistance [25,28,29]. At the same time, the present data refine this framework by showing that depletion of miR-199a-5p in the resistant state is not accompanied by a significant basal increase in XIAP at either mRNA or bulk protein level. This suggests that the resistant phenotype is not explained simply by constitutive XIAP overexpression, but by altered functional organisation of the axis.

This became clearer in the functional assays. In cisplatin-sensitive A2780 cells, miR-199a-5p retained its ability to repress XIAP under basal conditions, consistent with its proposed tumour-suppressive role [13]. Cisplatin also reduced XIAP levels in these cells, in agreement with previous studies linking chemotherapy-induced apoptosis to modulation of the XIAP/IAP axis [30–32]. At phenotypic level, this setting was characterised by reduced viability and increased apoptotic readouts under treatment, with the combined effect of miR-199a-5p and cisplatin being numerically consistent with an additive response rather than a strong cooperative interaction. Taken together, these findings support a model in which miR-199a-5p contributes to cisplatin responsiveness in

sensitive cells while remaining functionally aligned with XIAP repression and apoptotic execution. This pattern is compatible with threshold-based models of miRNA action, in which modest changes in regulatory input alter pathway responsiveness without necessarily generating interaction effects across all readouts [33].

By contrast, the resistant A2780cis model showed a different functional configuration. In these cells, miR-199a-5p enhanced caspase-3/7 activation without producing a corresponding reduction in XIAP protein levels under treatment conditions. This contrasts with the pattern observed in A2780 cells, in which basal XIAP repression by miR-199a-5p was preserved and cisplatin-associated responses remained more closely linked to apoptotic output. In A2780cis, restoration of miR-199a-5p therefore remained functionally relevant, but its effect was no longer adequately reflected by XIAP abundance alone. These findings indicate that, in resistant cells, the relationship between miR-199a-5p, XIAP and apoptotic output is reconfigured rather than lost.

This interpretation is consistent with previous work in ovarian cancer. miR-199a has been linked not only to drug response but also to broader signalling pathways, including HIF-1α- and NF-κB-associated networks [25,34] both of which are closely related to hypoxic adaptation, inflammatory survival signalling and chemotherapy response. In this setting, the absence of a measurable reduction in XIAP does not indicate loss of miR-199a-5p activity in resistant cells. Rather, it suggests that the effects of miR-199a-5p restoration may be distributed across a broader regulatory network in which apoptotic responsiveness can change even when the canonical target does not show a proportional change at bulk protein level. This interpretation is also supported by studies showing that stress conditions can alter miRNA behaviour, including changes in translational control [35,36], thereby weakening a simple relationship between miRNA abundance and target protein levels. In resistant cells, miR-199a-5p therefore appears to remain biologically active, but its output is no longer fully represented by XIAP repression alone.

The divergence between the apoptosis assays further supports this view. Whereas western blotting detected only modest changes in cleaved caspase-3, single-cell imaging showed a clearer increase in caspase-3/7 activation, particularly in the resistant line. This indicates that population-averaged assays may under-represent treatment-responsive subpopulations that are more readily detected at cell level [37]. The data therefore support the presence of a measurable apoptotic component within the resistant phenotype that becomes more apparent at single-cell resolution. This is consistent with the broader view of resistant ovarian cancer as a heterogeneous and dynamically organised state rather than a uniform condition of fixed resistance [1,3,4]. Within this framework, miR-199a-5p appears capable of modulating apoptotic competence in resistant cells even in the absence of a marked reduction in bulk XIAP protein.

The human tissue analysis extended this interpretation into a spatially resolved setting. In non-neoplastic ovary, the segregation between relatively stromal miR-199a-5p signal and epithelial XIAP enrichment is consistent with a compartmental organisation in which regulatory input and target-associated signal remain spatially separated. This interpretation is in keeping with previous evidence that miRNA programmes within the

ovarian stromal compartment are biologically relevant and can be remodelled during tumour-associated reprogramming [38]. In HGSOC, this organisation was altered. Both signals showed broader spatial overlap, together with redistribution of signal intensity and quantitative inversion of K1/K2 values accompanied by increased M1. These findings indicate a change in the spatial relationship between miR-199a-5p and XIAP rather than a simple increase in signal abundance. This is consistent with spatial studies showing that ovarian cancer behaviour and treatment response are influenced not only by cellular composition, but also by tissue architecture and the spatial arrangement of tumour-associated states [3,4,39]. The present data therefore extend spatial analyses of ovarian cancer to a miRNA–protein regulatory axis and indicate that the effective behaviour of the miR-199a-5p/XIAP relationship depends, at least in part, on compartmental and subcellular context within tumour tissue.

Overlap between miR-199a-5p and XIAP signal should not, however, be taken as evidence of effective repression. The tumour-associated increase in overlap, together with the altered contribution of XIAP to colocalised regions, is more consistent with a setting in which relative abundance, spatial competition and compartmental constraints influence the effective output of the axis [33,40,41]. Within this framework, the greater XIAP contribution within overlapping regions may reflect a condition in which target availability exceeds the effective repressive capacity of the local miRNA pool [42]. This interpretation provides a coherent link between the in vitro and tissue-level findings: in both settings, miR-199a-5p remains present and functionally relevant, but its relationship with XIAP output is non-linear and increasingly constrained by context. Tumour-associated 3'UTR shortening [43] represents one possible mechanism by which miRNA responsiveness could be further modified in this setting.

The altered subcellular pattern of miR-199a-5p adds a further layer to this reconfiguration. In HGSOC cells, miR-199a-5p showed prominent perinuclear and occasional nuclear-associated localisation, a pattern not observed in non-neoplastic control tissue. This finding extends the interpretation beyond tissue-level organisation alone. Nuclear trafficking of mature miRNAs is an active and regulated process [44], and nuclear miRNA functions are now well recognised [9,10,45,46]. In this context, the tumour-associated redistribution of miR-199a-5p indicates that subcellular compartmentalisation may influence not only where the miRNA is detected, but also how its regulatory activity is expressed. The present data do not define the mechanistic basis of this pattern, but they show that the biology of the axis extends beyond bulk abundance and includes tumour-associated changes in intracellular distribution.

Overall, the present findings support a model in which the miR-199a-5p/XIAP axis functions as a context-dependent regulatory system shaped by cellular state, treatment exposure and spatial organisation. In sensitive cells, miR-199a-5p remains functionally aligned with XIAP repression and apoptotic responsiveness. In resistant cells, that alignment is reconfigured, such that apoptotic output remains modifiable even when XIAP abundance does not change in parallel. In human HGSOC tissue, this reconfiguration is accompanied by altered spatial overlap and subcellular redistribution, indicating that the biological behaviour of the axis depends not only on abundance but also on architectural

and intracellular context. The main implication of this study is therefore not only that miR-199a-5p targets XIAP, but that the effective activity of this interaction is itself dynamically organised in ovarian cancer.

CONCLUSION

This study identifies a context-dependent reconfiguration of the miR-199a-5p/XIAP axis in ovarian cancer, in which the relationship between miR-199a-5p, XIAP and apoptotic output differs between cisplatin-sensitive and cisplatin-resistant states and is further shaped by spatial organisation in human HGSOC tissue. Our data indicate that miR-199a-5p abundance alone is insufficient to predict functional activity, highlighting the limitations of bulk expression-based approaches for assessment of miRNA-mediated regulation. By integrating functional assays with spatially resolved analysis, this work supports a framework in which miRNA activity is determined by regulatory context rather than expression level alone. These findings provide a basis for improving interpretation of miRNA-mediated phenotypes in ovarian cancer and support further investigation of spatially organised regulatory vulnerabilities associated with chemoresistance.

BIBLIOGRAPHY

1. Miras I, Estévez-García P, Muñoz-Galván S. Clinical and molecular features of platinum resistance in ovarian cancer. Crit Rev Oncol Hematol. septiembre de 2024;201:104434. doi:10.1016/j.critrevonc.2024.104434 PubMed PMID: 38960218.

2. Wagner V, Morton M, Dorayappan KDP, Gonzalez A, Yu L, Sakaue T, et al. Circulating extracellular vesicles protein expression for early prediction of platinum-resistance in high-grade serous ovarian cancer. Oncogene. mayo de 2025;44(17):1197-203. doi:10.1038/s41388-025-03382-4 PubMed PMID: 40210758; PubMed Central PMCID: PMC12015105.

3. Denisenko E, de Kock L, Tan A, Beasley AB, Beilin M, Jones ME, et al. Spatial transcriptomics reveals discrete tumour microenvironments and autocrine loops within ovarian cancer subclones. Nat Commun. 3 de abril de 2024;15(1):2860. doi:10.1038/s41467-024-47271-y PubMed PMID: 38570491; PubMed Central PMCID: PMC10991508.

4. Laury AR, Zheng S, Aho N, Fallegger R, Hänninen S, Saez-Rodriguez J, et al. Opening the Black Box: Spatial Transcriptomics and the Relevance of Artificial Intelligence-Detected Prognostic Regions in High-Grade Serous Carcinoma. Mod Pathol. julio de 2024;37(7):100508. doi:10.1016/j.modpat.2024.100508 PubMed PMID: 38704029.

5. Nunes M, Bartosch C, Abreu MH, Richardson A, Almeida R, Ricardo S. Deciphering the Molecular Mechanisms behind Drug Resistance in Ovarian Cancer to Unlock Efficient Treatment Options. Cells. 4 de mayo de 2024;13(9):786. doi:10.3390/cells13090786 PubMed PMID: 38727322; PubMed Central PMCID: PMC11083313.

6. Cetraro P, Plaza-Diaz J, MacKenzie A, Abadía-Molina F. A Review of the Current Impact of Inhibitors of Apoptosis Proteins and Their Repression in Cancer. Cancers (Basel). 25 de marzo de 2022;14(7):1671. doi:10.3390/cancers14071671 PubMed PMID: 35406442; PubMed Central PMCID: PMC8996962.

7. Jiang C, Shen C, Ni M, Huang L, Hu H, Dai Q, et al. Molecular mechanisms of cisplatin resistance in ovarian cancer. Genes Dis. noviembre de 2024;11(6):101063. doi:10.1016/j.gendis.2023.06.032 PubMed PMID: 39224110; PubMed Central PMCID: PMC11367050.

8. Atiaa AG, Abd E-Kader SM, Ellakwa DES. Crosstalk between microRNA and oxidative stress in ovarian cancer: diagnosis, pathogenesis and therapeutic resistance. Med Oncol. 27 de diciembre de 2025;43(2):104. doi:10.1007/s12032-025-03024-5 PubMed PMID: 41455858; PubMed Central PMCID: PMC12743700.

9. Hu X, Yin G, Zhang Y, Zhu L, Huang H, Lv K. Recent advances in the functional explorations of nuclear microRNAs. Front Immunol. 2023;14:1097491. doi:10.3389/fimmu.2023.1097491 PubMed PMID: 36911728; PubMed Central PMCID: PMC9992549.

10. Billi M, De Marinis E, Gentile M, Nervi C, Grignani F. Nuclear miRNAs: Gene Regulation Activities. Int J Mol Sci. 31 de mayo de 2024;25(11):6066. doi:10.3390/ijms25116066 PubMed PMID: 38892257; PubMed Central PMCID: PMC11172810.

11. Wang W, Alvero A, Qin Y, Wang M, Fox A, Li Y, et al. Engineered extracellular vesicles enriched with the miR-214/199a cluster enhance the efficacy of chemotherapy in ovarian cancer. Mol Oncol. 13 de febrero de 2026. doi:10.1002/1878-0261.70224 PubMed PMID: 41685760.

12. Lian XY, Zhang H, Liu Q, Lu X, Zhou P, He SQ, et al. Ovarian cancer-excreted exosomal miR-199a-5p suppresses tumor metastasis by targeting hypoxia-inducible factor-2α in hypoxia microenvironment. Cancer Commun (Lond). agosto de 2020;40(8):380-5. doi:10.1002/cac2.12034 PubMed PMID: 32428376; PubMed Central PMCID: PMC7427304.

13. Muñoz-Galdeano T, Reigada D, Soto A, Barreda-Manso MA, Ruíz-Amezcua P, Nieto-Díaz M, et al. Identification of a New Role of miR-199a-5p as Factor Implied in Neuronal Damage: Decreasing the Expression of Its Target X-Linked Anti-Apoptotic Protein (XIAP) After SCI. International Journal of Molecular Sciences. enero de 2024;25(22):12374. doi:10.3390/ijms252212374

14. Rennie W, Kanoria S, Liu C, Carmack CS, Lu J, Ding Y. Sfold Tools for MicroRNA Target Prediction. Methods Mol Biol. 2019;1970:31-42. doi:10.1007/978-1-4939-9207-2_3 PubMed PMID: 30963486.

15. Livak KJ, Schmittgen TD. Analysis of relative gene expression data using real-time quantitative PCR and the 2(-Delta Delta C(T)) Method. Methods. diciembre de 2001;25(4):402-8. doi:10.1006/meth.2001.1262 PubMed PMID: 11846609.

16. Headrick TC. Statistical Simulation: Power Method Polynomials and Other Transformations. New York: Chapman and Hall/CRC; 2009. 174 p. doi:10.1201/9781420064919

17. Søe MJ, Møller T, Dufva M, Holmstrøm K. A sensitive alternative for microRNA in situ hybridizations using probes of 2'-O-methyl RNA + LNA. J Histochem Cytochem. julio de 2011;59(7):661-72. doi:10.1369/0022155411409411 PubMed PMID: 21525189; PubMed Central PMCID: PMC3201160.

18. Chi SW, Zang JB, Mele A, Darnell RB. Argonaute HITS-CLIP decodes microRNA-mRNA interaction maps. Nature. 23 de julio de 2009;460(7254):479-86. doi:10.1038/nature08170 PubMed PMID: 19536157; PubMed Central PMCID: PMC2733940.

19. Hafner M, Landthaler M, Burger L, Khorshid M, Hausser J, Berninger P, et al. Transcriptome-wide identification of RNA-binding protein and microRNA target sites by PAR-CLIP. Cell. 2 de abril de 2010;141(1):129-41. doi:10.1016/j.cell.2010.03.009 PubMed PMID: 20371350; PubMed Central PMCID: PMC2861495.

20. Sung H, Ferlay J, Siegel RL, Laversanne M, Soerjomataram I, Jemal A, et al. Global Cancer Statistics 2020: GLOBOCAN Estimates of Incidence and Mortality Worldwide for 36 Cancers in 185 Countries. CA Cancer J Clin. mayo de 2021;71(3):209-49. doi:10.3322/caac.21660 PubMed PMID: 33538338.

21. Lheureux S, Gourley C, Vergote I, Oza AM. Epithelial ovarian cancer. Lancet. 23 de marzo de 2019;393(10177):1240-53. doi:10.1016/S0140-6736(18)32552-2 PubMed PMID: 30910306.

22. Cremona M, Vandenberg CJ, Farrelly AM, Madden SF, Morgan C, Kalachand R, et al. BRCA mutations lead to XIAP overexpression and sensitise ovarian cancer to inhibitor of apoptosis (IAP) family inhibitors. Br J Cancer. agosto de 2022;127(3):488-99. doi:10.1038/s41416-022-01823-5

23. Kandettu A, Adiga D, Devi V, Suresh PS, Chakrabarty S, Radhakrishnan R, et al. Deregulated miRNA clusters in ovarian cancer: Imperative implications in personalized medicine. Genes Dis. 1 de marzo de 2022;9(6):1443-65. doi:10.1016/j.gendis.2021.12.026 PubMed PMID: 36157483; PubMed Central PMCID: PMC9485269.

24. Kinose Y, Sawada K, Nakamura K, Sawada I, Toda A, Nakatsuka E, et al. The hypoxia-related microRNA miR-199a-3p displays tumor suppressor functions in ovarian carcinoma. Oncotarget. 10 de mayo de 2015;6(13):11342-56. doi:10.18632/oncotarget.3604 PubMed PMID: 25839163; PubMed Central PMCID: PMC4484460.

25. Feng X, Liu N, Deng S, Zhang D, Wang K, Lu M. miR-199a modulates cisplatin resistance in ovarian cancer by targeting Hif1α. Onco Targets Ther. 2017;10:5899-906. doi:10.2147/OTT.S145833 PubMed PMID: 29276393; PubMed Central PMCID: PMC5731338.

26. Friedman RC, Farh KKH, Burge CB, Bartel DP. Most mammalian mRNAs are conserved targets of microRNAs. Genome Res. enero de 2009;19(1):92-105. doi:10.1101/gr.082701.108 PubMed PMID: 18955434; PubMed Central PMCID: PMC2612969.

27. Kertesz M, Iovino N, Unnerstall U, Gaul U, Segal E. The role of site accessibility in microRNA target recognition. Nat Genet. octubre de 2007;39(10):1278-84. doi:10.1038/ng2135 PubMed PMID: 17893677.

28. Wang Z, Ting Z, Li Y, Chen G, Lu Y, Hao X. microRNA-199a is able to reverse cisplatin resistance in human ovarian cancer cells through the inhibition of mammalian target of rapamycin. Oncol Lett. septiembre de 2013;6(3):789-94. doi:10.3892/ol.2013.1448 PubMed PMID: 24137412; PubMed Central PMCID: PMC3789061.

29. Liu MX, Siu MKY, Liu SS, Yam JWP, Ngan HYS, Chan DW. Epigenetic silencing of microRNA-199b-5p is associated with acquired chemoresistance via activation of JAG1-Notch1 signaling in ovarian cancer. Oncotarget. 28 de febrero de 2014;5(4):944-58. doi:10.18632/oncotarget.1458 PubMed PMID: 24659709; PubMed Central PMCID: PMC4011596.

30. Asselin E, Mills GB, Tsang BK. XIAP regulates Akt activity and caspase-3-dependent cleavage during cisplatin-induced apoptosis in human ovarian epithelial cancer cells. Cancer Res. 1 de marzo de 2001;61(5):1862-8. PubMed PMID: 11280739.

31. Li J, Feng Q, Kim JM, Schneiderman D, Liston P, Li M, et al. Human Ovarian Cancer and Cisplatin Resistance: Possible Role of Inhibitor of Apoptosis Proteins*This work was supported by grants from the Canadian Institutes of Health Research (MOP-15691), the University of Ottawa-Industry Grants Program, and the Ottawa Civic Hospital Foundation. Endocrinology. 1 de enero de 2001;142(1):370-80. doi:10.1210/endo.142.1.7897

32. He X, Khurana A, Maguire JL, Chien J, Shridhar V. HtrA1 sensitizes ovarian cancer cells to cisplatin-induced cytotoxicity by targeting XIAP for degradation. Int J Cancer. 1 de marzo de 2012;130(5):1029-35. doi:10.1002/ijc.26044 PubMed PMID: 21387310; PubMed Central PMCID: PMC3206182.

33. Mukherji S, Ebert MS, Zheng GXY, Tsang JS, Sharp PA, van Oudenaarden A. MicroRNAs can generate thresholds in target gene expression. Nat Genet. 21 de agosto de 2011;43(9):854-9. doi:10.1038/ng.905 PubMed PMID: 21857679; PubMed Central PMCID: PMC3163764.

34. Chen R, Alvero AB, Silasi DA, Kelly MG, Fest S, Visintin I, et al. Regulation of IKKbeta by miR-199a affects NF-kappaB activity in ovarian cancer cells. Oncogene. 7 de agosto de 2008;27(34):4712-23. doi:10.1038/onc.2008.112 PubMed PMID: 18408758; PubMed Central PMCID: PMC3041589.

35. Bhattacharyya SN, Habermacher R, Martine U, Closs EI, Filipowicz W. Relief of microRNA-mediated translational repression in human cells subjected to stress. Cell. 16 de junio de 2006;125(6):1111-24. doi:10.1016/j.cell.2006.04.031 PubMed PMID: 16777601.

36. Vasudevan S, Tong Y, Steitz JA. Switching from repression to activation: microRNAs can up-regulate translation. Science. 21 de diciembre de 2007;318(5858):1931-4. doi:10.1126/science.1149460 PubMed PMID: 18048652.

37. Marusyk A, Almendro V, Polyak K. Intra-tumour heterogeneity: a looking glass for cancer? Nat Rev Cancer. 19 de abril de 2012;12(5):323-34. doi:10.1038/nrc3261 PubMed PMID: 22513401.

38. Mitra AK, Zillhardt M, Hua Y, Tiwari P, Murmann AE, Peter ME, et al. MicroRNAs reprogram normal fibroblasts into cancer-associated fibroblasts in ovarian cancer. Cancer Discov. diciembre de 2012;2(12):1100-8. doi:10.1158/2159-8290.CD-12-0206 PubMed PMID: 23171795; PubMed Central PMCID: PMC3685866.

39. Stur E, Corvigno S, Xu M, Chen K, Tan Y, Lee S, et al. Spatially resolved transcriptomics of high-grade serous ovarian carcinoma. iScience. 18 de marzo de 2022;25(3):103923. doi:10.1016/j.isci.2022.103923 PubMed PMID: 35252817; PubMed Central PMCID: PMC8891954.

40. Denzler R, McGeary SE, Title AC, Agarwal V, Bartel DP, Stoffel M. Impact of MicroRNA Levels, Target-Site Complementarity, and Cooperativity on Competing Endogenous RNA-Regulated Gene Expression. Mol Cell. 3 de noviembre de 2016;64(3):565-79. doi:10.1016/j.molcel.2016.09.027 PubMed PMID: 27871486; PubMed Central PMCID: PMC5101187.

41. Salmena L, Poliseno L, Tay Y, Kats L, Pandolfi PP. A ceRNA hypothesis: the Rosetta Stone of a hidden RNA language? Cell. 5 de agosto de 2011;146(3):353-8. doi:10.1016/j.cell.2011.07.014 PubMed PMID: 21802130; PubMed Central PMCID: PMC3235919.

42. Zinchuk V, Zinchuk O, Okada T. Quantitative colocalization analysis of multicolor confocal immunofluorescence microscopy images: pushing pixels to explore biological phenomena. Acta Histochem Cytochem. 30 de agosto de 2007;40(4):101-11. doi:10.1267/ahc.07002 PubMed PMID: 17898874; PubMed Central PMCID: PMC1993886.

43. Mayr C, Bartel DP. Widespread shortening of 3'UTRs by alternative cleavage and polyadenylation activates oncogenes in cancer cells. Cell. 21 de agosto de

2009;138(4):673-84. doi:10.1016/j.cell.2009.06.016 PubMed PMID: 19703394; PubMed Central PMCID: PMC2819821.

44. Wei Y, Li L, Wang D, Zhang CY, Zen K. Importin 8 regulates the transport of mature microRNAs into the cell nucleus. J Biol Chem. 11 de abril de 2014;289(15):10270-5. doi:10.1074/jbc.C113.541417 PubMed PMID: 24596094; PubMed Central PMCID: PMC4036152.

45. Catalanotto C, Cogoni C, Zardo G. MicroRNA in Control of Gene Expression: An Overview of Nuclear Functions. Int J Mol Sci. 13 de octubre de 2016;17(10):1712. doi:10.3390/ijms17101712 PubMed PMID: 27754357; PubMed Central PMCID: PMC5085744.

46. El Fatimy R, Zhang Y, Deforzh E, Ramadas M, Saravanan H, Wei Z, et al. A nuclear function for an oncogenic microRNA as a modulator of snRNA and splicing. Mol Cancer. 15 de enero de 2022;21(1):17. doi:10.1186/s12943-022-01494-z PubMed PMID: 35033060; PubMed Central PMCID: PMC8760648.

ADDITIONAL INFORMATION

Ethics approval and consent to participate
This study was approved by the Clinical Research Ethics Committee of the Complejo Hospitalario de Toledo (CEIm No. 968). Written informed consent was obtained from all participants prior to inclusion in the study. All procedures involving human participants were performed in accordance with the ethical standards of the institutional research committee and with the Declaration of Helsinki.

Consent for publication
Not applicable.

Availability of data and materials
The datasets generated and/or analysed during the current study are available from the corresponding author on reasonable request.

Competing interests
The authors declare no competing interests.

Funding
This work was supported by Fundación Eurocaja Rural through the "Ayudas Sociales" programme (2022 and 2025), and by the Consejería de Educación, Cultura y Deportes de la Junta de Comunidades de Castilla-La Mancha, co-financed by the European Union through FEDER ("A way to make Europe"), under project references SBPLY/17/000376 and SBPLY/21/180501/000097.

Authors' contributions

T.M.-G. conceived and designed the study, acquired and analysed data, interpreted the results, drafted the original manuscript, and revised the final version. D.R. and M.N.-D. contributed to data analysis and critically revised the manuscript. M.P.K., L.G.G., M.G.P. and B.S. contributed to patient recruitment, sample provision, clinical data collection, clinical interpretation, and critical revision of the manuscript. G.I. contributed to computational analysis, information systems, data processing, AI-based methodological development, and critical revision of the manuscript. R.M.M. conceived and designed the study, interpreted the results, supervised the study, and critically revised the manuscript. All authors approved the final version of the manuscript and agree to be accountable for all aspects of the work.

Acknowledgements

The authors are deeply grateful to Dr. J.A. Rodríguez Alfaro and Dr. J. Mazarío from the Microscopy and Image Analysis Core Facilities of the National Hospital for Paraplegics, Toledo, for their outstanding technical support and expertise in microscopy and image analysis, which substantially contributed to this work.

A.

```
5'->3'          G      AAUU    CC          U
Target  2198    GAAUA     GUU    AUGCUGG    2218
                |||||     |||    |||||||
miRNA     23    CUUGU     CAG    UGUGACC    1
3'->5'                CCAU    ACU         C
```

ΔG_{hybrid} = -15.4 Kcal/mol

B.

```
5'->3'          U    AA      AA         U
Target   628     ACA   UGG C   AACACUG    645
                 |||   ||| |   |||||||
miRNA     23     UGU   AUC G   UUGUGAC    1
3'->5'          CU    CC    A AC         CC
```

ΔG_{hybrid} = -15.2 Kcal/mol

C.

miRNA	Site_Position	LogitProb†	Score	ΔGhybrid
hsa-miR-199a-5p	2198-2218	0.543	0.234	-15.400

D.

E.

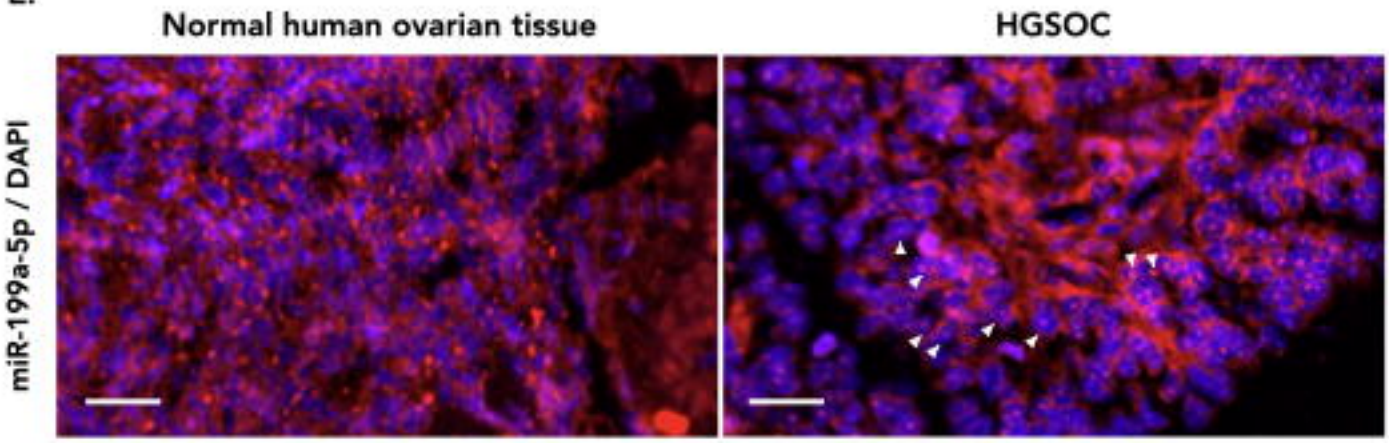

A. Normal human ovarian tissue

B. HGSOC human tissue

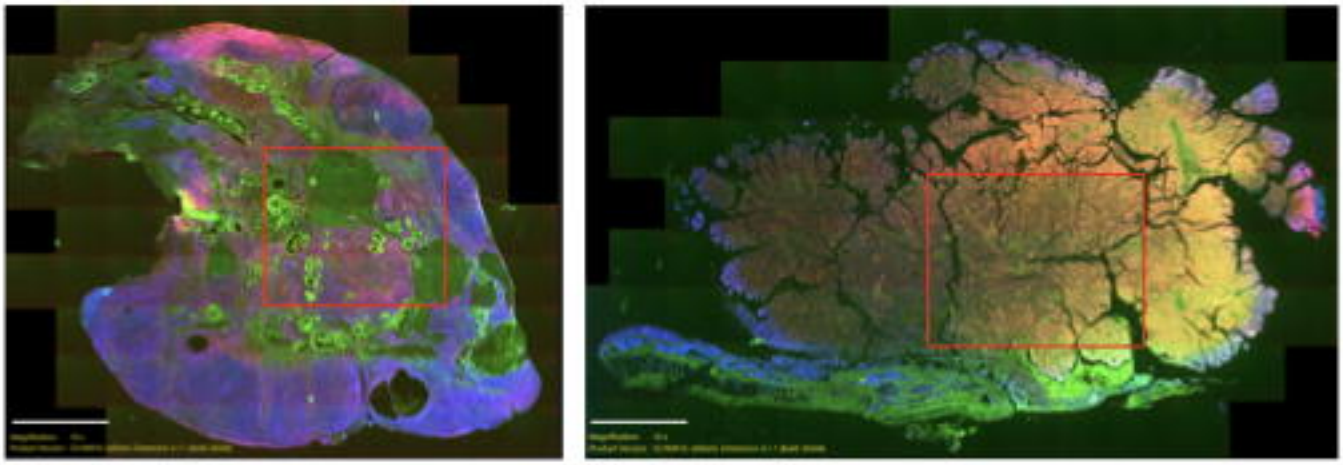

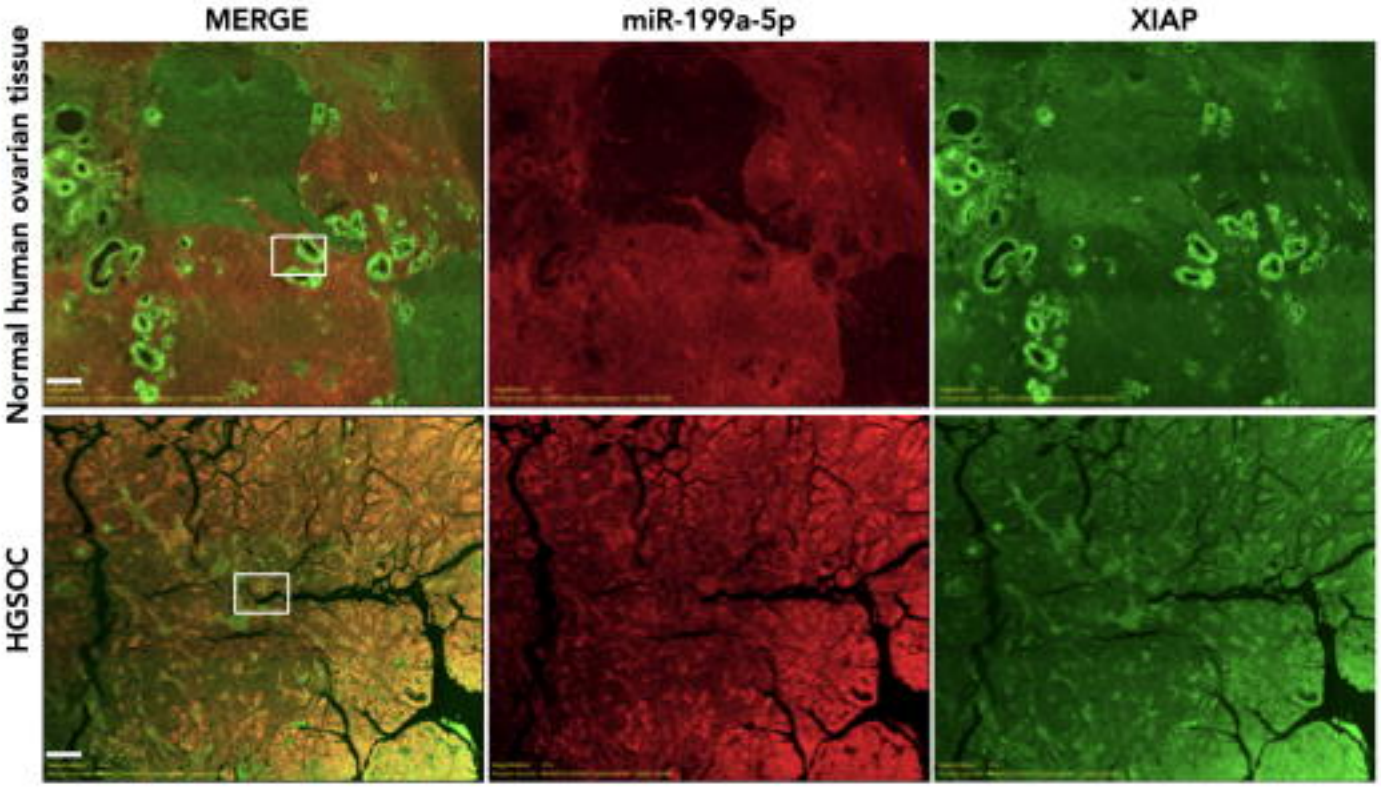

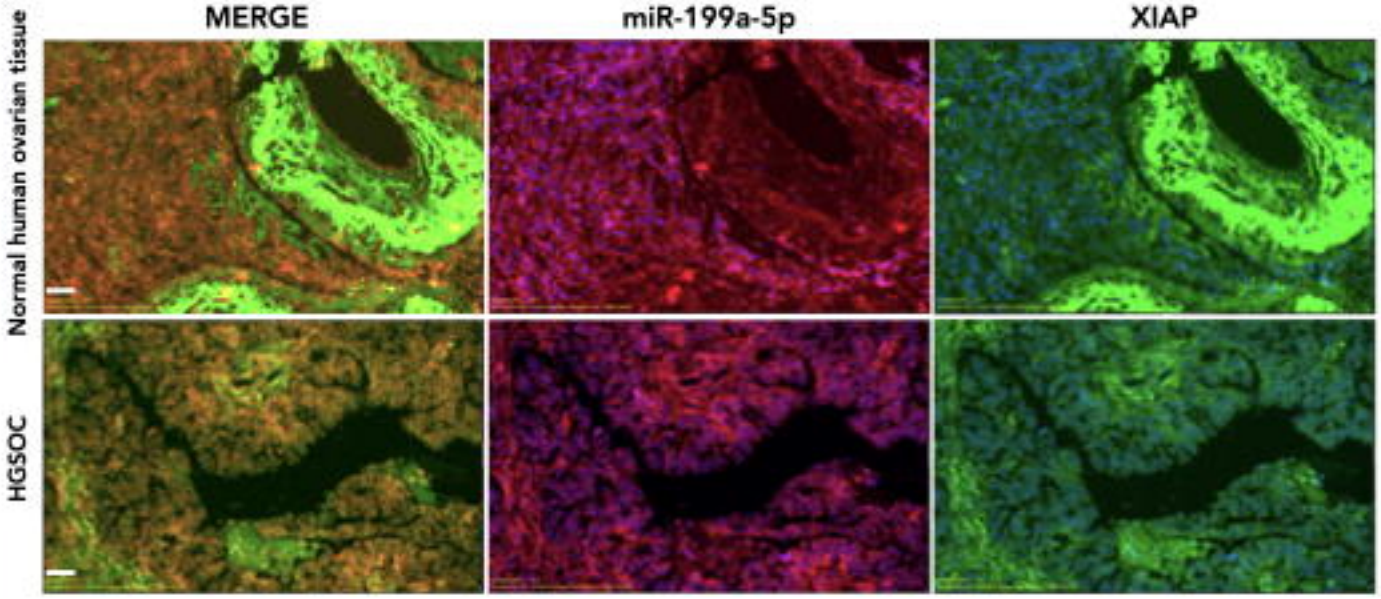

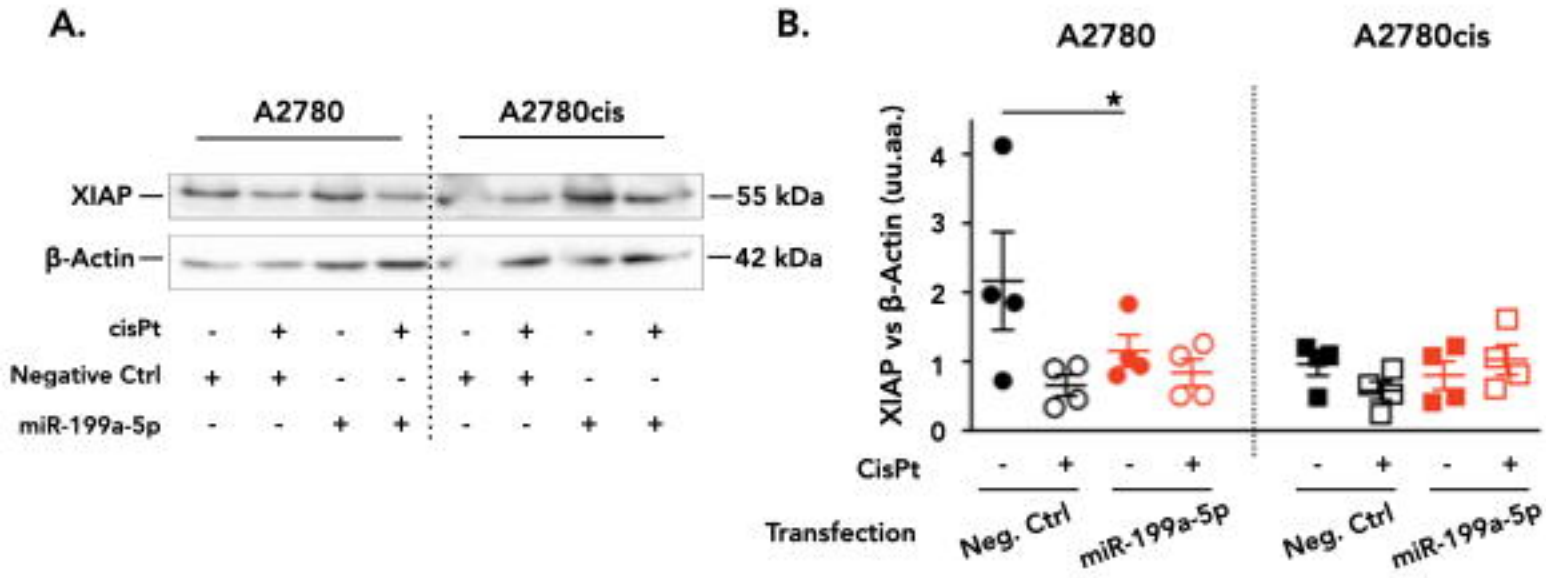
A.
A2780
A2780cis
XIAP
β-Actin
55 kDa
42 kDa
cisPt
Negative Ctrl
miR-199a-5p
B.
A2780
A2780cis
XIAP vs β-Actin (uu.aa.)
CisPt
Transfection
Neg. Ctrl
miR-199a-5p

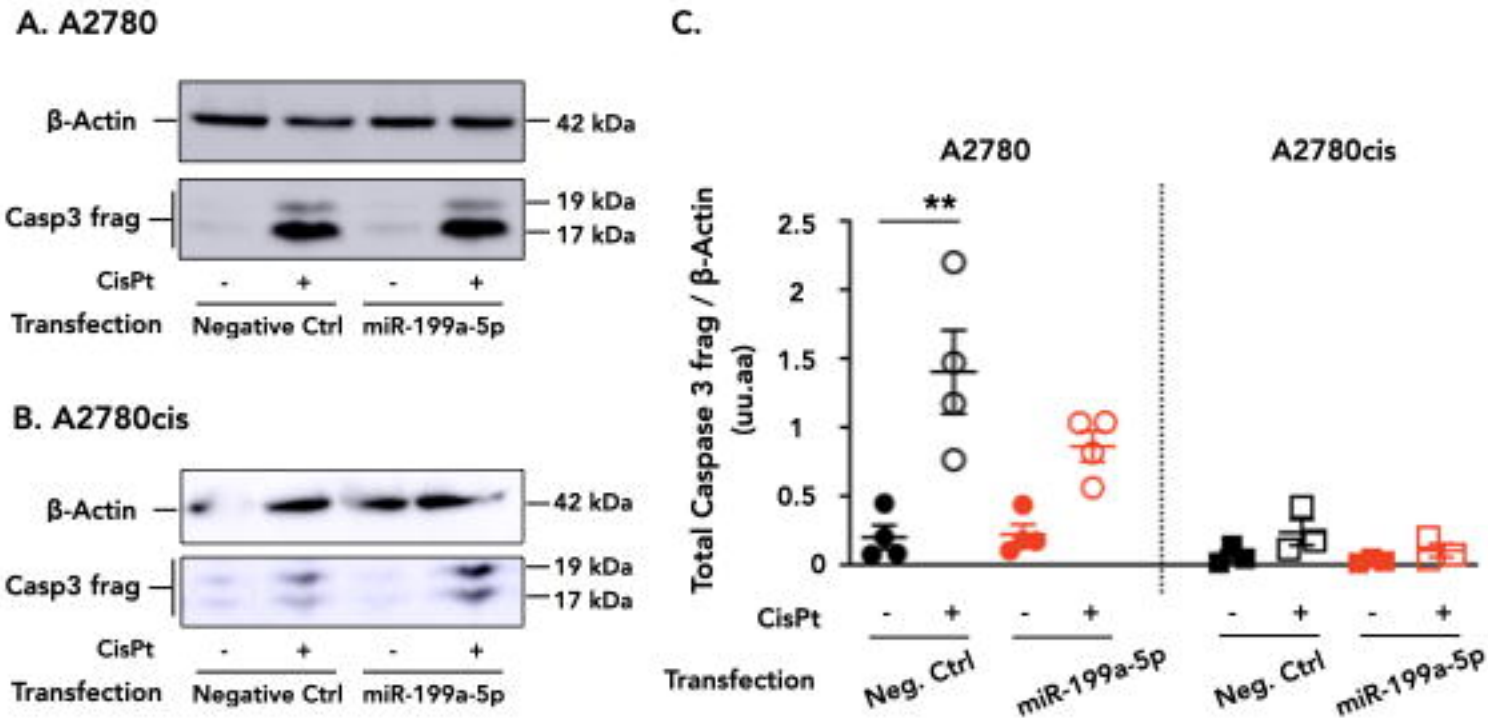
A. A2780
β-Actin
42 kDa
Casp3 frag
19 kDa
17 kDa
CisPt
-
+
-
+
Transfection
Negative Ctrl
miR-199a-5p
B. A2780cis
β-Actin
42 kDa
Casp3 frag
19 kDa
17 kDa
CisPt
-
+
-
+
Transfection
Negative Ctrl
miR-199a-5p
C.
A2780
A2780cis
Total Caspase 3 frag / β-Actin (uu.aa)
**
2.5
2
1.5
1
0.5
0
CisPt
Transfection
Neg. Ctrl
miR-199a-5p
Neg. Ctrl
miR-199a-5p

A.

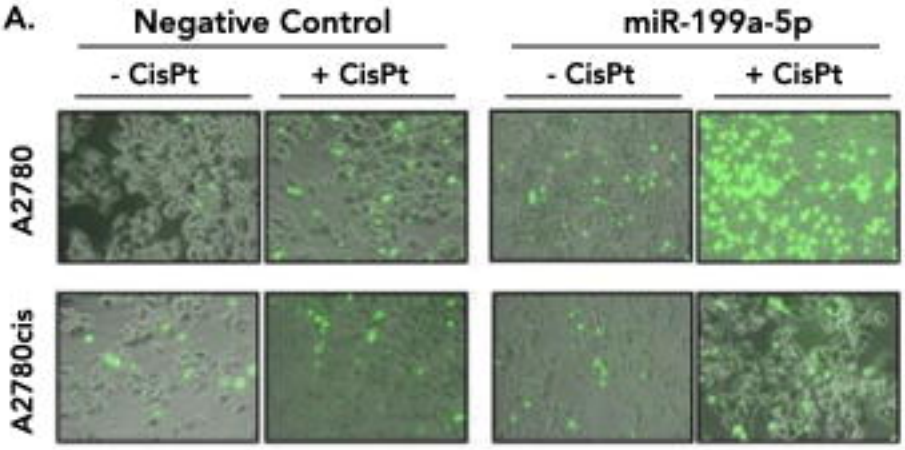
Negative Control
miR-199a-5p
- CisPt
+ CisPt
- CisPt
+ CisPt
A2780
A2780cis

B.

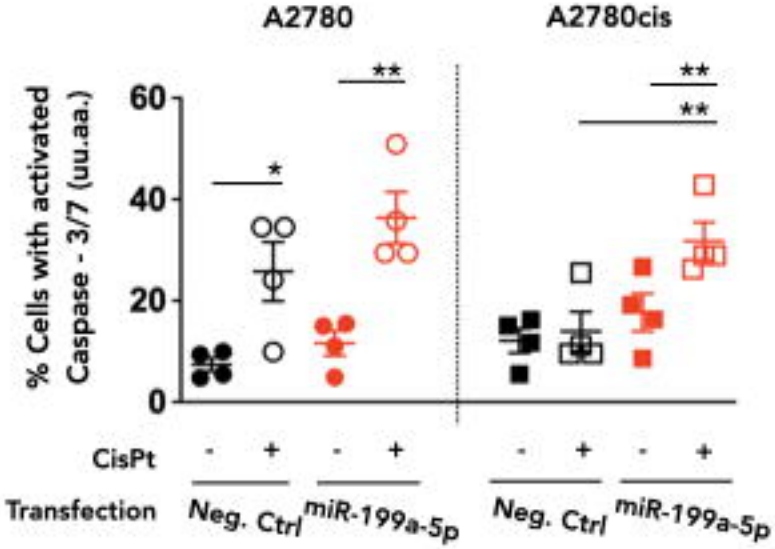
A2780
A2780cis
% Cells with activated Caspase - 3/7 (uu.aa.)
60
40
20
0
*
**
**
**
CisPt
- + - +
- + - +
Transfection
Neg. Ctrl
miR-199a-5p
Neg. Ctrl
miR-199a-5p

A.

A2780

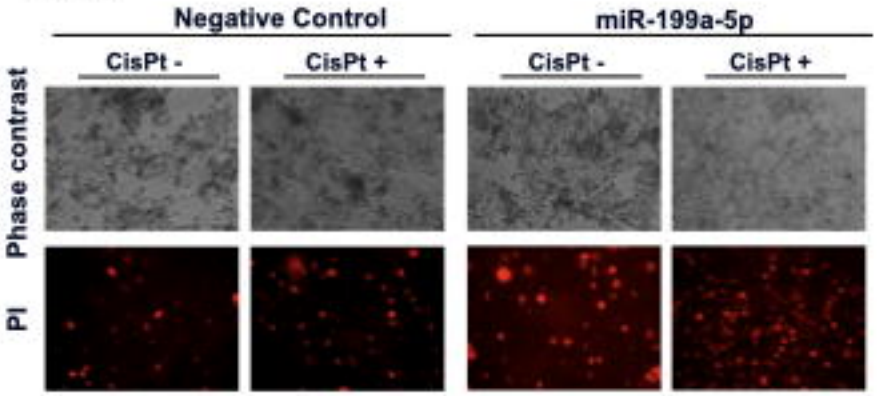

B.

A2780cis

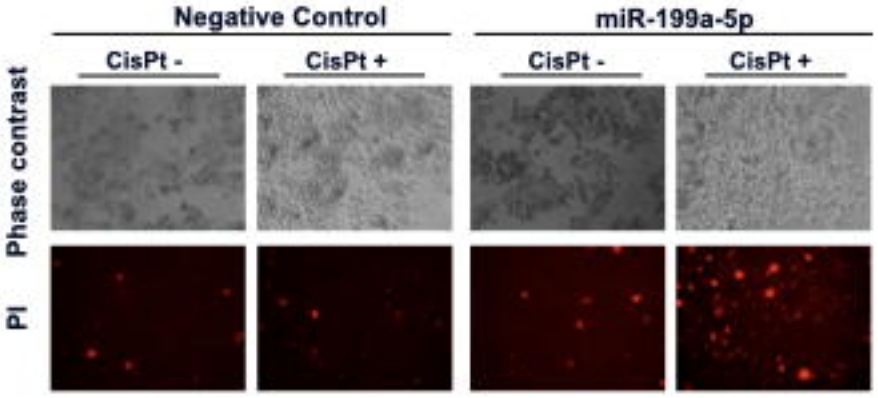

C.

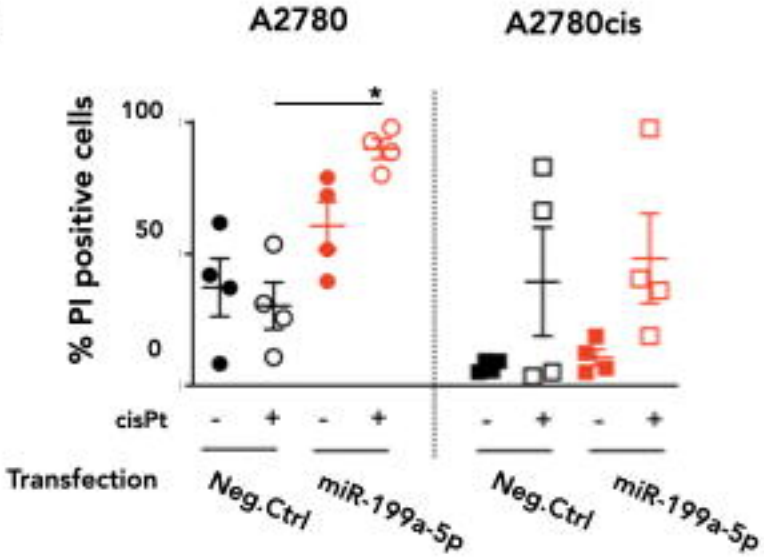

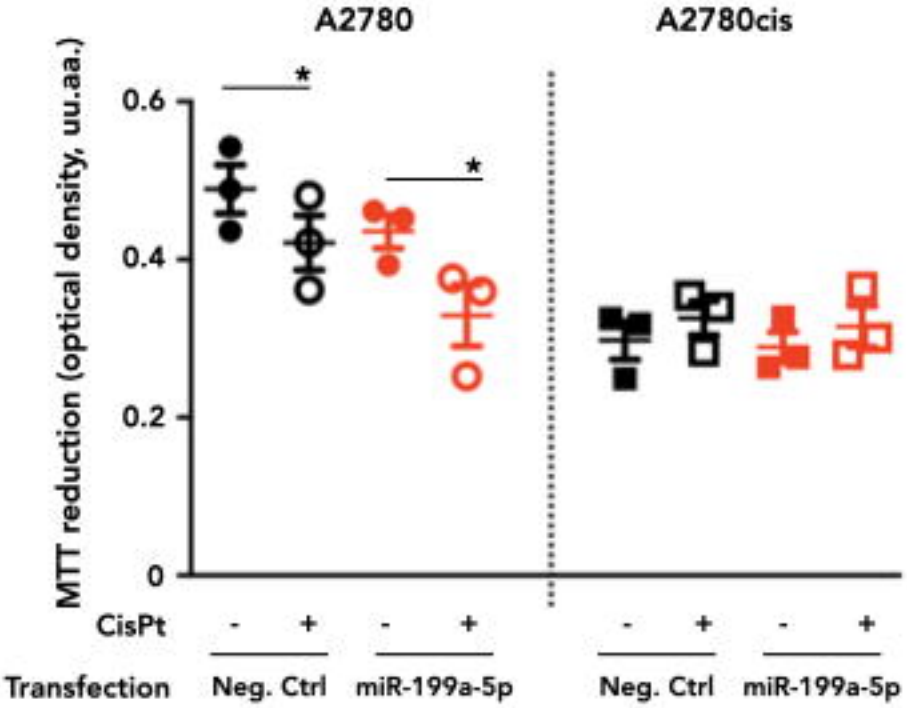
A2780
A2780cis
MTT reduction (optical density, uu.aa.)
0.6
0.4
0.2
0
*
*
CisPt
-
+
-
+
-
+
-
+
Transfection
Neg. Ctrl
miR-199a-5p
Neg. Ctrl
miR-199a-5p

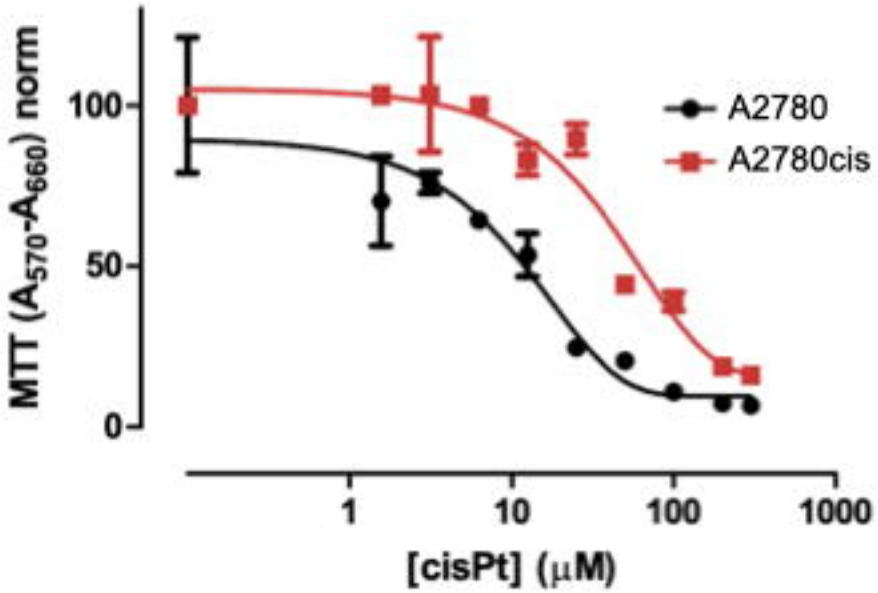
MTT (A_{570}-A_{660}) norm
100
50
0
1
10
100
1000
[cisPt] (μM)
A2780
A2780cis

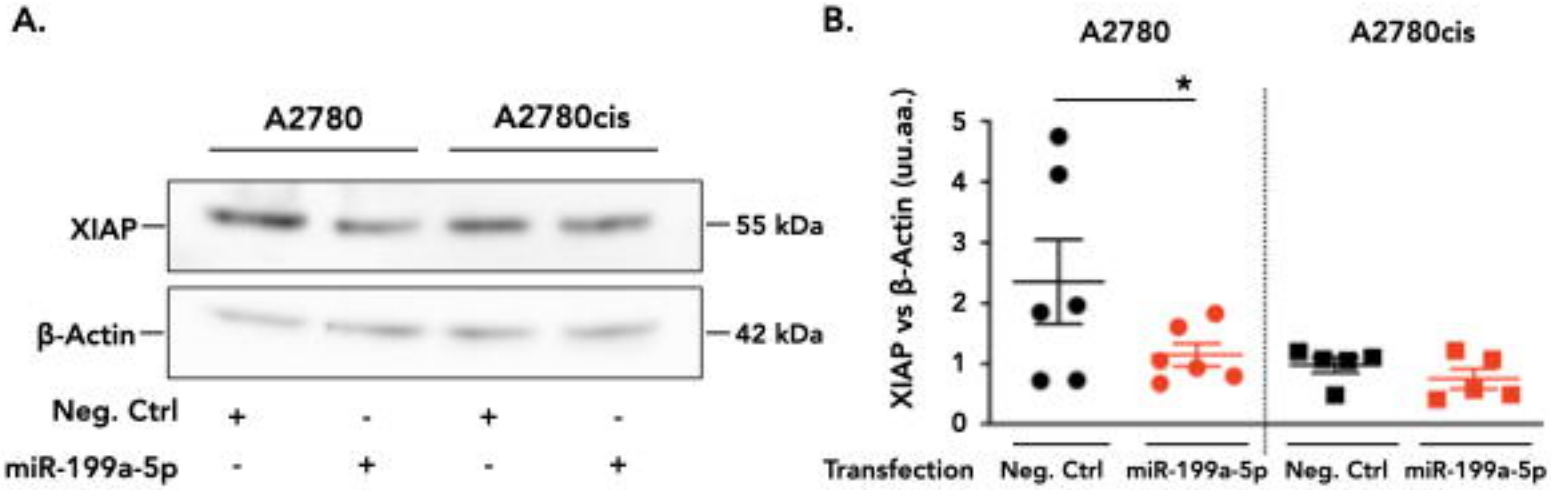
A.
A2780
A2780cis
XIAP
β-Actin
55 kDa
42 kDa
Neg. Ctrl
miR-199a-5p
B.
A2780
A2780cis
XIAP vs β-Actin (uu.aa.)
Transfection
Neg. Ctrl
miR-199a-5p
Neg. Ctrl
miR-199a-5p

A.

	ΔCt	T-test			fold decrease	
		mean diff (ΔΔCt)		p value		
A2780	3.89 ± 0.41	**A2780 vs. A2780 cis**	2.55 (0.27, 2.41)	$T_4 = 3.46$	5.85	(0.83 , 10.63)
A2780 cis	6.44 ± 2.11			**p = 0.013 (*)**		

	ΔCt	T-test			fold increase	
		mean diff (ΔΔCt)		p value		
A2780	13.001 ± 0.63	**A2780 vs. A2780 cis**	-0.472 (-1.656 , 0.712)	$T_4 = 1.106$	1.387	(0.61 , 3.151)
A2780 cis	12.53 ± 0.232			p = 0.165		

B.

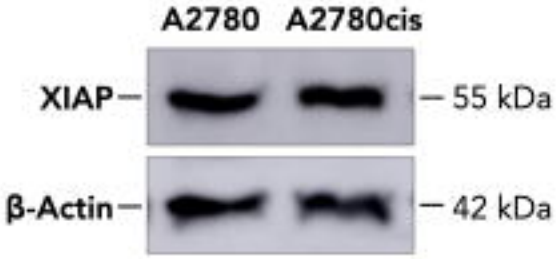

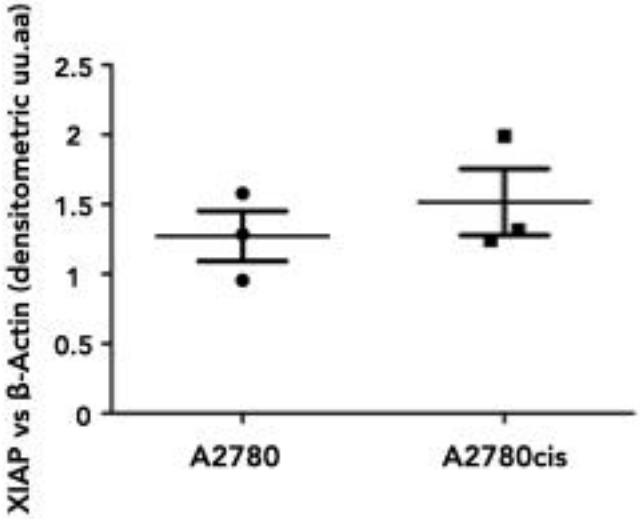
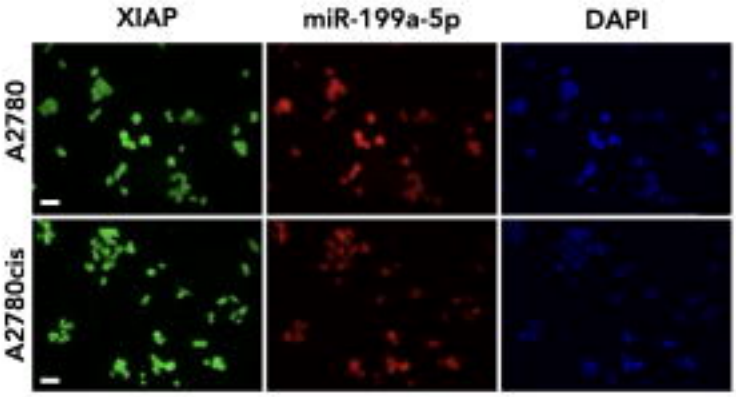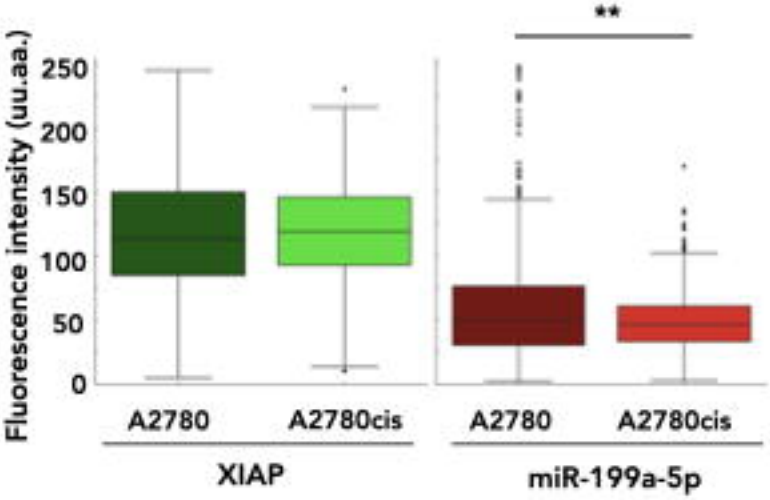
C.